Mathematical Modelling of Inertial Migration in Periodic Microcentrifuge Devices Using Regular Perturbation

Zeinab Rahnama

Confirmation proposal
September 2026

Abstract

(incomplete) Cavity-based microcentrifuges use recirculating flow beside a microchannel to separate and retain suspended particles and cells, and to exchange the fluid surrounding them. Experiments demonstrate size-selective capture, but a 2D vortex image cannot predict whether a particle will enter a cavity or remain there. The background flow is 3D, and finite particles can move relative to the fluid. This project combines 3D background-flow calculations with a finite-particle model to study these processes.

The work completed to date includes steady finite-element solutions and a topological analysis of the background flow in a periodic channel–cavity cell. The periodic formulation is the principal model. A fully developed Poiseuille inlet provides an inlet–outlet reference, while a quadratic inlet provides a secondary sensitivity case. All three use the same target upstream mean velocity and flux. Fixed-depth critical points, their continued branches, local eigenvalues and selected 3D fluid trajectories reveal changes in flow structure with Reynolds number.

Contents

1 Introduction **1**

1.1 Motivation 1
1.2 Research problem 2
1.3 Research questions 2
1.4 Aim and objectives 3
1.5 Scope and present status 4
1.6 Structure of the proposal 4

2 Background and Research Gap **5**

2.1 Foundations of inertial migration in straight ducts 5
2.2 3D channel–cavity background flow 8
2.3 Microcentrifuge experiments and particle-transport models 9
2.4 Research gap 10
2.5 Mathematical formulation 11
2.5.1 Geometry and notation 12
2.5.2 Full fluid equations and physical boundary conditions 13
2.5.3 Background flow and the exact disturbance equation 14
2.5.4 Disturbance boundary conditions and particle domain choice . . 16
2.5.5 Laboratory time dependence 17
2.5.6 Mean velocity nondimensionalisation 19
2.5.7 Particle scales and regular perturbation 20
2.5.8 Hydrodynamic loads and particle motion 23

3 Methodology **26**

3.1 Computational geometry and particle meshes 26
3.2 Flow normalisation and flux verification 26
3.3 Boundary condition and forcing implementation 27
3.4 Background-flow discretisation and verification 27
3.5 Background-flow topology analysis 28
3.6 Preliminary particle method 30

3.6.1 Staged development and verification 31
3.6.2 Leading motion and matrix conventions 32
3.6.3 Existing reference calculation and proposed verification case . . 34
3.6.4 Staged adaptation of the particle calculation 35
3.7 Planned stationary-device-frame inertial correction; under assessment . 36

4 Results to Date **37**
4.1 Background-flow verification 37
4.2 Fixed-depth background-flow structure 38
4.3 Principal centre-track 42
4.4 Depthwise velocity on the centre-track 46
4.5 In-plane eigenvalues and provisional transition intervals 48
4.6 Low-Reynolds number boundary-formulation comparison 50
4.7 3D reconstruction and boundary-formulation comparison at Reynolds number 100 53
4.8 Preliminary one-particle Stokes results 55

5 Discussion **56**
5.1 What the background results establish 56
5.2 Boundary formulation and common flow scale 56
5.3 Meaning and limitations of the particle result 57
5.4 Limits and next steps 57

6 Conclusions and Planned Work **58**
6.1 Conclusions from work completed to date 58
6.2 Staged research plan and validation gates 59
6.3 Expected research outputs 59

Chapter 1

Introduction

1.1 Motivation

Controlling the motion of suspended particles and cells is important in microfluidic applications, including blood-cell separation and the isolation of rare circulating tumour cells [1,2]. Microfluidic devices can use fluid motion and channel geometry to manipulate these suspensions within compact systems. Understanding how particles respond to the flow is therefore important for predicting and improving device operation [3].

Inertial microfluidics uses fluid inertia effects to manipulate particles. One such effect is lateral migration in pressure-driven channel flow: fluid inertia can generate a cross-stream hydrodynamic force on a neutrally buoyant rigid sphere, causing it to migrate towards preferred positions within the channel [4, 5]. The resulting migration depends on particle size and hydrodynamic interactions with the surrounding flow and channel walls [6]. This dependence provides a physical basis for size-selective particle manipulation and motivates mathematical models of particle motion in confined flows [3].

Devices containing repeated expansions and contractions can create recirculating flow regions alongside the main channel. Hur *et al.* [7] demonstrated preferential capture of larger particles and cells in expansion reservoirs under suitable operating conditions, and Mach *et al.* [8] used this principle for automated cellular sample preparation. These applications motivate questions about particle transport: what determines whether a particle passes a cavity, enters it, remains inside, or returns to the main channel? Answering these questions requires understanding how the cavity flow interacts with a particle of finite size.

The mathematical challenge is to relate the 3D fluid flow to the translation and rotation of a finite particle. The flow varies spatially through each expansion and contraction, so a moving particle encounters changing hydrodynamic conditions even when the particle-free flow is steady [9]. A predictive model must therefore assess

trapping, motion relative to the surrounding fluid, and acceleration within a consistent formulation. This motivates the present numerical investigation of the 3D background flow and the development of a stationary-device-frame particle model. Together, these provide a basis for investigating how flow strength, particle size and initial position influence migration, cavity entry, retention and release.

1.2 Research problem

A cavity microcentrifuge couples through-flow in the main channel to flow in an adjoining expansion cavity. When 3D recirculation develops, a non-zero depthwise velocity can carry fluid trajectories between fixed-depth planes [10, 11]. A planar vortex or a fixed-depth streamline plot therefore cannot determine the complete 3D transport. Furthermore, a finite inertial particle does not generally follow a background-fluid streamline: its translation and rotation depend on its finite size, position relative to the boundaries, the spatially varying background flow and the disturbance it creates [6, 9]. Background-flow topology alone is therefore insufficient to predict particle behaviour.

The modelling problem has two coupled levels. The first is to obtain a 3D background field with a clearly defind velocity scale, boundary conditions and quantified numerical uncertainty. The second is to resolve a finite sphere in that flow and develop a particle-motion model from its disturbance equations in the stationary device frame. The model must account consistently for finite-size effects, disturbance evolution and particle acceleration. The travelling wave approximation used in the singularity model of Christensen and Roper [9] provides a relevant point of comparison; its applicability to the present resolved-sphere formulation requires assessmnet.

1.3 Research questions

The work is organised around the following questions.

RQ1: At a common target mean velocity, which fixes the nominal Reynolds number and flux for the chosen fluid and channel cross-section, how do streamwise-periodic and inlet–outlet formulations affect the 3D background flow?

RQ2: How does local and global background-flow structure change with Reynolds number, and which conclusions are supported by fixed-depth diagnostics, 3D trajectories and numerical sensitivity tests?

RQ3: Can a particle model with an explicitly resolved sphere be developed, numerically verified and physically validated in the statoinary device frame, beginning at

$\mathrm{Re} = 10$, and under what conditions is its first-order disturbance approximation acurate?

RQ4: At $\mathrm{Re} = 10$, how do initial position and particle radius, together with the resulting proximity to walls, affect passage, entry, residence, retention and release within the validated model range?

RQ5: Where a higher-Reynolds-number particle model can be validated, how do changes in the background flow affect the boundaries between particle outcomes, and where does the proposed first-order regular-perturbation approximation cease to be adequate?

1.4 Aim and objectives

The overall aim is to develop and validate a mathematical framework for inertial migration and possible retention of finite-sized particles in a periodic channel–cavity microcentrifuge, using inlet–outlet calculations as background-flow references. The work connects verified 3D background fields, a proposed regular-perturbation model with an explicitly resolved sphere, and particle trajectories.

The objectives are to:

1. calculate the 3D background flow for the periodic cell and inlet–outlet reference problems under a common mean-velocity convention, and assess the applicability of the steady-flow assumption at higher Reynolds numbers;

2. verify the background calculations through solver, bulk-flow, boundary-condition mesh and sampling checks, and assess the sensitivity of derived trajectories and diagnostics;

3. characterise Reynolds-number-dependent flow structure using fixed-depth critical points, a continued root branch, local linear diagnostics and selected 3D fluid trajectories;

4. complete and verify the leading finite-particle resistance and mobility calculations at symmetry and off-centre positions;

5. finalise the first-order closure from the exact disturbance equations, implement the complete particle correction, verify its numerical balances and assess its accuracy against suitable particle-resolved reference calculations;

6. calculate particle trajectories over selected positions, radii and flow conditions within the validated range, using an interpolated particle-velocity field only where the closure supports it, and classfy the resulting events and outcomes;

7. compare predicted trends with experiments and existing simulations while accounting for differences in geometry, particle properties and Reynolds-number definitions.

1.5 Scope and present status

The initial particle study considers rigid spheres in an incompressible Newtonian fluid, with neutral buoyancy as the reference case. These calculations provide a controlled model for the transport mechanisms motivating the biomedical applications; quantitative application to cells requires separate assessment of their deformability and other relevant properties.

The background solver and topology-analysis procedures have been implemented. The periodic $\mathrm{Re} = 10$ medium-source field has passed the reported bulk-flow, periodicity and volume checks, while source-mesh refinement remains incomplete. The periodic–Poiseuille comparisons at $\mathrm{Re} = 10$ and 100 have been quantified for the base-resolution sampled fields (Sections 4.6 and 4.7). At $\mathrm{Re} = 100$, closed orbits have also been computed in the interpolated fields.

Preliminary particle calculations at $\boldsymbol{x}_p = (0, -0.5, 0)$, $\kappa = 0.05$ and $\mathrm{Re} = 10$ provide evidence for the leading Stokes resistance and mobility calculation at one symmetry position. The complete physical inertial correction remains under development. Particle trajectories, entry boundaries, stable particle orbits and retention maps are planned results contingnt on validation of that correction and the resulting trajectory model.

1.6 Structure of the proposal

Chapter 2 reviews the relevant literature, defines the mathematical formulation and identifies the research gap. It distinguishes the exact fluid and particle equations from the proposed disturbance-time approximation and regular-perturbation model. Chapter 3 describes the numerical procedures and verification strategy. Chapter 4 reports the background-flow results and preliminary one-particle Stokes calculations. Chapter 5 interprets the supported findings and their limitations. Chapter 6 summarises the contribution and presents the staged research plan and acceptance criteria.

Chapter 2

Background and Research Gap

2.1 Foundations of inertial migration in straight ducts

The experiments of Segré and Silberberg [4] showed that neutrally buoyant rigid spheres in pipe Poiseuille flow migrate across streamlines and accumulate on an off-axis annulus. Because the undisturbed, fully developed pipe flow has no radial velocity, this observation shows that a finite particle can acquire a cross-stream velocity that is absent from the local background flow. In the corresponding creeping-flow problem, a single rigid, neutrally buoyant, force- and torque-free sphere in steady, fully developed Newtonian Poiseuille flow has no lateral migration. This follows from Stokes-flow reversibility together with the symmetries of the sphere and straight-duct geometry [12,13]. The migration observed by Segré and Silberberg [4] therefore requires fluid inertia. Ho and Leal [5] subsequently analysed the analogous low-inertia problem in plane Poiseuille flow and predicted a stable off-centre equilibrium position.

An early theoretical result relevant to inertial lift is the analysis of Saffman [12], who considered a sphere translating parallel to the undisturbed streamlines in an unbounded linear shear flow. The slip is measured relative to the undisturbed fluid velocity at the sphere centre. Dimensional variables are used in the following lift-force scalings. If V_s is the slip-speed magnitude and G is the shear-rate magnitude, Saffman's lift-force magnitude has the characteristic scaling

$$F_{\mathrm{S}} \sim 6.46\,\mu a^2 V_s \left(\frac{G}{\nu}\right)^{1/2}, \tag{2.1}$$

where a is the particle radius and μ and ν are the dynamic and kinematic viscosities, respectively. This result applies in the shear-dominated limit $\mathrm{Re}_s \ll \mathrm{Re}_G^{1/2} \ll 1$, where $\mathrm{Re}_s = V_s a/\nu$ and $\mathrm{Re}_G = Ga^2/\nu$ [12,14]. Note that, the numerical prefactor in Saffman's

original publication was subsequently corrected from 81.2 to 6.46 [14]. For a fixed orientation of the shear, the transverse force acts towards streamlines moving opposite to the particle's slip; reversing the shear reverses the transverse direction. The result demonstrates how slip, shear, and weak fluid inertia combine to generate a transverse force. The displayed linear-shear formula does not account for channel walls or the curvature of a Poiseuille velocity profile.

Cox and Brenner [15] developed a general low-inertia framework that accounted for the background flow and solid boundaries. Ho and Leal [5] subsequently calculated the inertial migration of a small neutrally buoyant sphere in bounded plane Poiseuille flow and predicted a stable off-centre equilibrium. In the small-particle, low-channel-Reynolds-number regime, a signed lateral-force component has the leading form [5, 6]

$$F_L = \rho U_m^2 \frac{a^4}{L_d^2} \left[C_L \left(\frac{\boldsymbol{x}_\perp}{L_d} \right) + O\left(\frac{a}{L_d} \right) \right], \tag{2.2}$$

where ρ is the fluid density, L_d is a characteristic duct dimension, $\boldsymbol{x}_\perp$ is the particle-centre position in the cross-section, and C_L is a signed dimensionless coefficient. Here U_m is chosen as the maximum speed of the undisturbed duct flow, distinct from the mean velocity U_b used later in the present formulation. At this leading order, C_L is independent of a as $a/L_d \to 0$, with dimensionless position and geometry held fixed. The force therefore scales as a^4 where the leading coefficient is nonzero; higher-order size corrections can become important near its zeros [6].

Vasseur and Cox [16] applied the Cox–Brenner framework to spherical particles between parallel walls, including plane Poiseuille flow. Later studies examined different Reynolds-number orderings. Using the present scales, with U_m denoting the maximum speed of the undisturbed flow and a the particle radius, the channel Reynolds number is $\mathrm{Re}_c = U_m L_d/\nu$. The particle Reynolds number based on the characteristic shear rate U_m/L_d is $\mathrm{Re}_p = U_m a^2/(\nu L_d) = \mathrm{Re}_c (a/L_d)^2$ [6, 13].

Schonberg and Hinch [13] considered a small sphere with channel Reynolds number of order unity and small particle Reynolds number. Asmolov [17] extended the analysis to large channel Reynolds numbers while retaining the small-particle-Reynolds-number assumption. These studies show that small particle Reynolds number can coexist with channel Reynolds number of order unity or larger, while inertia remains important in the particle-disturbed flow. Both analyses use matched asymptotic expansions [13, 17]; small particle Reynolds number alone therefore does not establish the validity of a regular perturbation throughout a channel–cavity domain.

The extension to a 3D straight duct is particularly relevant to the present work. Hood *et al.* [6] developed an asymptotic model for a rigid sphere in Poiseuille flow through a square duct. The undisturbed flow remains unidirectional, but its speed

depends on both cross-sectional coordinates. At the leading nonzero order in particle scale inertia, their componentwise small-particle expansion can be written in vector form as

$$\boldsymbol{F}_L = \rho U_m^2 \frac{a^4}{L_d^2}\left[\boldsymbol{C}_4\left(\frac{\boldsymbol{x}_\perp}{L_d}\right) + \frac{a}{L_d}\boldsymbol{C}_5\left(\frac{\boldsymbol{x}_\perp}{L_d}\right) + O\left(\frac{a^2}{L_d^2}\right)\right], \tag{2.3}$$

where L_d is now the square-duct side length. The coefficient fields are determined by the background flow, particle position, and confining geometry. The a^4 term gives the leading small-particle contribution, while the a^5 term provides the first finite-size correction. This is an expansion at the retained order in inertia, rather than an exact finite-Reynolds-number force law.

Here $\boldsymbol{F}_L$ denotes the lateral force evaluated with lateral particle motion suppressed, while streamwise translation and rotation are chosen to give zero streamwise force and torque [6]. Under a quasi-steady lift–drag balance, with no other lateral driving, the migration velocity satisfies $\boldsymbol{V}_\perp = \mathsf{M}_\perp \boldsymbol{F}_L$, where $\mathsf{M}_\perp$ is the lateral mobility tensor. For finite, nonsingular mobility, cross-sectional equilibrium positions therefore satisfy

$$\boldsymbol{F}_L(\boldsymbol{x}_\perp^*) = \boldsymbol{0}. \tag{2.4}$$

Only attracting equilibria act as stable focusing positions [6]. Local asymptotic stability follows when all eigenvalues of the linearised migration-velocity field have negative real parts; any eigenvalue with positive real part implies instability. If no eigenvalue has positive real part but at least one has zero real part, linearisation alone is inconclusive [18]. Focusing in a 3D duct thus depends on the complete migration-velocity field and boundary geometry. Wall- and shear-related contributions offer useful physical interpretations, but such decompositions depend on the geometry and asymptotic formulation rather than defining two universal force laws [17].

Straight-duct theory provides physical limits and benchmarks for the present particle model. A channel–cavity device, however, differs from a fully developed straight duct. Confined channel–cavity flows can vary through the expansion and develop 3D recirculation and fluid exchange with the main channel [11]. These features violate the streamwise-invariance and unidirectional-flow assumptions underlying the straight-duct theories. Their lift formulae and equilibrium structures therefore cannot be transferred directly to the cavity, although they remain useful benchmarks in sufficiently developed straight channel segments. Hood *et al.* [6, p. 471] identify the scaling of unsteady effects as an unresolved issue for extending their approach to non-rectilinear geometries, including microcentrifuges. Together, these considerations motivate a model of finite-particle motion in the three-dimensional background flow of the actual channel–cavity geometry, with any quasi-steady approximation explicitly justified.

2.2 3D channel–cavity background flow

A cavity beneath a channel can support recirculating flow, with the side walls introducing 3D motion. For a rectangular cavity beneath a channel, Torczynski and O'Hern [10] computed Reynolds-number-dependent streamline topologies involving spiral points and out-of-plane transport. At higher Reynolds numbers, they also described a dividing stream surface bounding an apparently isolated recirculating volume. Their numerical results and schematic interpretations provide a reference for the present analysis; the corresponding critical points, streamline connectivity, and any invariant surfaces must nevertheless be established from the velocity field computed for the present geometry and boundary conditions.

Experiments and simulations by Haddadi and Di Carlo [19] demonstrated spiralling flow that exchanges fluid between the main channel and a cavity's recirculating region. Khojah *et al.* [11] further investigated how recirculation development and fluid exchange depend on Reynolds number and cavity aspect ratio, reporting no evidence of isolated closed streamlines in the configurations examined. These findings show that a recirculating region in a 3D cavity need not be isolated from the main channel by the material barrier familiar from steady 2D cavity flow. They do not, however, establish that every 3D cavity lacks internal invariant regions. Whether exchanging and confined regions coexist must be determined for the particular geometry and flow conditions.

This distinction also governs the interpretation of planar flow visualisations. Integral curves of the in-plane velocity components at a fixed depth can reveal local flow structure, but they are not generally trajectories of the full 3D flow. For steady flow, they represent fluid trajectories only where the normal velocity remains zero along the curve; an invariant symmetry plane provides one such setting. Otherwise, fluid elements leave the displayed plane through their out-of-plane velocity. Consequently, a closed curve in a planar velocity plot does not by itself establish a closed 3D streamline or a material barrier to fluid exchange.

Fluid residence and finite-particle trapping must likewise be distinguished. Haddadi and Di Carlo [19] showed that an isolated finite-size particle can approach a stable orbit within a cavity that exchanges fluid with the main channel. In dynamical systems terminology, such an orbit represents an attracting limit cycle of the particle transport system. Conversely, a closed background-flow streamline is not sufficient to establish particle trapping because the motion of a finite inertial particle is not identical to passive fluid advection. The particle can develop slip relative to the undisturbed fluid and respond to velocity gradients, hydrodynamic interactions with boundaries, and inertial lift [19].

The Eulerian topology and Lagrangian transport structure of the particle-free

background flow should therefore first be characterised separately from the finite-particle dynamics. The resulting flow structures can then be compared with particle trajectories, attracting equilibria, and periodic orbits. In particular, finite-time particle residence within the cavity should be distinguished from asymptotically stable trapping; the limitations of finite observation intervals are explicitly discussed by Haddadi and Di Carlo [19, p. 446]. Finite-time residence indicates that a particle remains within a prescribed region over a finite observation interval. Here, asymptotically stable trapping denotes retention associated with an invariant set of the particle dynamics, such as an equilibrium or periodic orbit, whose particle positions remain within the cavity and which is both stable under sufficiently small perturbations and attracting to nearby particle states [18].

2.3 Microcentrifuge experiments and particle-transport models

Hur *et al.* [7] demonstrated a passive, size-based cell-enrichment device comprising eight parallel channels with repeated expansion–contraction reservoirs. Within the investigated trapping regime, larger particles and cells were preferentially retained in the reservoir vortices, while smaller cells predominantly passed downstream. The authors interpreted this behaviour in terms of upstream inertial focusing followed by size-dependent migration into the recirculating regions. Mach *et al.* [8] developed a related centrifuge-on-a-chip platform for automated cellular sample preparation and solution exchange. These experiments demonstrate practical size-selective capture. However, observation of particle retention over a finite interval does not, by itself, establish asymptotic stability of the retained particle motion [19, p. 446].

Particle-resolved studies have examined the dynamics underlying cavity trapping. Combining microfluidic experiments with lattice-Boltzmann simulations, Haddadi and Di Carlo [19] demonstrated 3D fluid exchange between a channel and its cavity recirculation region, while an isolated finite-size particle approached a stable limit-cycle orbit. Their numerical configuration employed streamwise-periodic boundary conditions. Jiang *et al.* [20] used a fully resolved immersed-boundary–lattice-Boltzmann method to investigate a single neutrally buoyant particle, reporting Reynolds-number-dependent trapping regimes, orbital motion, rotation, and escape. Their flow was driven by an inlet–outlet pressure difference, with pressure boundary conditions specified at the inlet and outlet [20, Sec. 2]. These studies establish that finite-particle trapping and stable orbital motion have already been investigated experimentally and numerically. They provide reference cases for the present work, although quantitative comparisons require

compatible geometries, particle properties, driving conditions, initial conditions, and Reynolds-number definitions.

Reduced models can decrease the computational cost of trajectory prediction within their asymptotic range of validity. Christensen *et al.* [21] developed a hybrid asymptotic–numerical method for inertial migration in straight channels of uniform but arbitrary cross-sectional shape. In a subsequent preprint, Christensen and Roper [9] applied a small-particle singularity formulation to microcentrifuge transport. Their particle-velocity model combines numerically computed background advection, an inertial migration contribution, and a Faxén finite-size correction, and predicts size-dependent capture thresholds and particle trajectories. The model was used to predict size-dependent capture thresholds and particle trajectories. The formulation employs a travelling-wave approximation for the disturbance; the authors discuss limitations associated with particle motion relative to device walls [9, Sec. II].

These existing models provide methodological and physical benchmarks for the present formulation. Relative to these singularity-based reduced models, the intended distinction is the treatment of a finite-radius sphere with explicit surface boundary conditions within a reduced disturbance formulation for the actual channel–cavity geometry, rather than the choice of reference frame alone. A consistent stationary-device-frame derivation must account for the dependence of the disturbance on particle configuration, including the time derivative induced by particle motion. Background-flow acceleration and particle translational and rotational inertia must be retained or consistently neglected according to the adopted asymptotic ordering. Wall boundary conditions, streamwise periodicity, and the choice between prescribed pressure-gradient forcing and prescribed volumetric flux must likewise be specified consistently. The accuracy and range of validity of the resulting model must then be established through verification and comparison with suitable reference solutions.

2.4 Research gap

Previous experiments, particle-resolved simulations, and reduced models have reported size-dependent cavity capture, stable particle orbits, and escape [9, 19, 20]. Building on these results, the present project addresses three linked questions concerning the selected channel–cavity geometry of Torczynski and O'Hern [10] and the chosen particle-modelling framework.

First, the sensitivity of the background-flow topology and cavity–channel exchange to the global boundary-value formulation remains to be quantified through a controlled comparison of finite inlet–outlet and streamwise-periodic domains. The comparison will use the same local channel–cavity geometry, fluid properties, reference length scale,

and target mean streamwise velocity U_b, defined over a specified unobstructed channel cross-section of area A_{ch}. These choices also fix the volumetric flux, $Q = U_b A_{\mathrm{ch}}$, and the Reynolds number, $Re = U_b H_c/\nu$. The complete inlet, outlet, wall, and periodic conditions, together with the axial domain dimensions, must be specified so that observed differences can be interpreted in terms of the global flow formulation. The pressure gradient required to maintain the matched throughput need not be identical in the two problems.

Second, the accuracy and range of validity of a first-order inertial particle-velocity model with an explicitly resolved spherical boundary must be established for the spatially varying, 3D cavity flow. Straight-duct theories and the Christensen–Roper microcentrifuge model provide reference limits and comparison cases [6, 9]. In the present formulation, particle motion changes the disturbance through its dependence on position relative to the background flow and device boundaries. Consequently, a steady background field does not imply a time-independent particle disturbance. The treatment of this configuration dependence and the associated time derivative must be derived consistently with the chosen inertial expansion, particle force and torque balances, and flow-driving constraint. The resulting correction requires numerical verification and assessment against appropriate reference solutions.

Third, the dependence of particle transport and retention on initial position, particle radius, and Reynolds number must be determined for the selected periodic geometry and model. This requires explicit criteria for direct passage, cavity entry, finite time residence, escape after entry, and stable retained motion. These criteria must distinguish trajectories from long-time dynamical states and specify the observation interval and evidence used to assess stability. In the periodic domain, passage must be defined relative to a reference cross-section or unwrapped streamwise coordinate; cavity escape and subsequent re-entry must be recorded separately. Trajectories that leave the numerical or asymptotic range of validity, including inadequately resolved near-wall motion, must be flagged separately from physical transport outcomes.

The intended contribution is a quantitative account of how the verified background flow and finite-particle hydrodynamic response combine to determine passage, cavity residence, and retention in the selected device. This requires verification of both the background flow and particle model, together with clearly defined trajectory criteria, estimates of numerical uncertainty, and an assessment of asymptotic validity.

2.5 Mathematical formulation

The formulation decomposes the fluid velocity into a steady, 3D particle-free background flow and a generally time-dependent disturbance generated by a moving rigid sphere.

This section defines the geometry, governing equations, and force and torque balances that determine the particle motion. It distinguishes the exact disturbance formulation from the proposed approximation for the disturbance time derivative and the subsequent regular-perturbation expansion. Numerical solution and verification procedures are described in Chapter 3.

Throughout the particle formulation, $\boldsymbol{u}_{\mathrm{tot}}$ denotes the total fluid velocity, $\overline{\boldsymbol{u}}$ the particle-free background velocity, and $\boldsymbol{v}$ the disturbance, so that $\boldsymbol{u}_{\mathrm{tot}} = \overline{\boldsymbol{u}} + \boldsymbol{v}$. In the background-flow topology analysis (Section 3.5) and the associated background-flow results and figure captions, the scalar symbols (u, v, w) denote the streamwise, vertical and depthwise components of $\overline{\boldsymbol{u}}$, respectively. The scalar v in that component notation is distinct from the disturbance vector $\boldsymbol{v}$.

2.5.1 Geometry and notation

Let x be streamwise, y vertical and z depthwise. Hats denote dimensional quantities, and spatial coordinates are nondimensionalised by the vertical cavity depth $\widehat{H}_c$:

$$\boldsymbol{x} = \frac{\widehat{\boldsymbol{x}}}{\widehat{H}_c}. \tag{2.5}$$

The origin lies at the centre of the cavity mouth in the plane $z = 0$. One periodic cell occupies $-L_p/2 \le x \le L_p/2$, with $L_p = 3$. The upper channel extends over $0 \le y \le H$, while the cavity occupies $-1 \le y \le 0$ beneath the opening $-L/2 \le x \le L/2$. Both regions have the same full depthwise width W, so that $-W/2 \le z \le W/2$.

The dimensionless cavity depth, upper-channel height, cavity length, and full depthwise width are $H_c = 1$, $H = 0.5$, $L = 1$, and $W = 2.125$, respectively. The open main channel cross sectional area and side-wall locations are therefore

$$A_{\mathrm{ch}} = HW = \frac{17}{16} = 1.0625, \qquad z_{\mathrm{wall}} = \pm\frac{W}{2} = \pm 1.0625. \tag{2.6}$$

Here A_{ch} is dimensionless, with $\widehat{A}_{\mathrm{ch}} = \widehat{H}_c^2 A_{\mathrm{ch}}$.

These geometric ratios follow Torczynski and O'Hern [10], who denote the vertical cavity depth by D, the channel height by h, and the depthwise half-width by W. The present notation uses W for the full depthwise width and places the streamwise origin at the centre of the cavity mouth. The periodic formulation identifies the faces $x = \pm L_p/2$, denoted by $\Gamma_{\pm}$; the original report instead considers an inlet–outlet problem.

A rigid sphere of dimensional radius $\widehat{a}$ has centre $\widehat{\boldsymbol{x}}_p(\widehat{t})$, translational velocity $\widehat{\boldsymbol{U}}_p$,

and angular velocity $\widehat{\boldsymbol{\Omega}}_p$. Its dimensionless radius and centre position are

$$\kappa = \frac{\widehat{a}}{\widehat{H}_c}, \qquad \boldsymbol{x}_p = \frac{\widehat{\boldsymbol{x}}_p}{\widehat{H}_c}. \tag{2.7}$$

The particle-containing fluid domain is obtained by removing the sphere from the device domain and therefore depends on the particle position. The sphere is assumed not to intersect the solid walls. The proposed verification sphere is positioned above the cavity mouth, halfway through the upper-channel height, and away from the depthwise symmetry plane. The selected depthwise offset will be recorded with the calculation inputs. The particle-free background flow is defined throughout the device, including the volume subsequently occupied by the sphere.

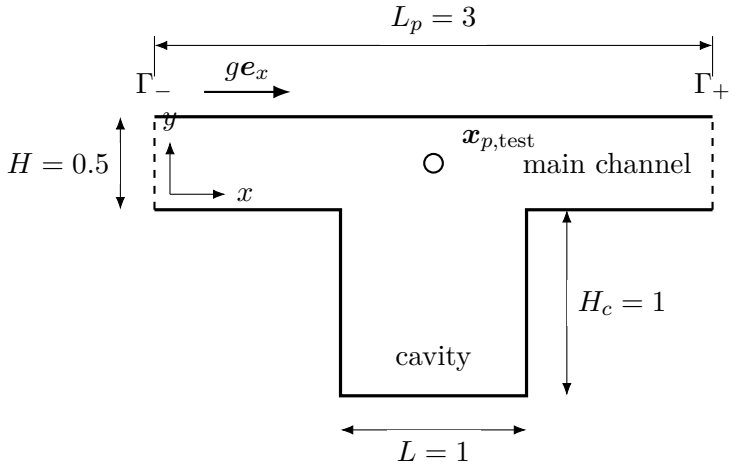


Figure 2.1: Projection of the channel–cavity geometry onto the x–y plane. Solid lines denote solid walls, and dashed lines denote the paired streamwise faces $\Gamma_\pm$ at $x = \pm L_p/2$ for the periodic formulation. The arrow indicates the pressure-gradient forcing $g\boldsymbol{e}_x$, defined in the governing equations. The circle shows the projected verification sphere at $\boldsymbol{x}_{p,\mathrm{test}} = (0, 0.25, z_{\mathrm{test}})$, with $z_{\mathrm{test}} \neq 0$ and dimensionless radius $\kappa = 0.05$. It does not represent a section through the off-centre sphere at $z = 0$. The selected depthwise offset will be recorded with the calculation inputs. The background flow is calculated without the sphere. The full depthwise domain is $-W/2 \leq z \leq W/2$.

2.5.2 Full fluid equations and physical boundary conditions

The particle model starts from the fluid motion in the presence of the sphere. The total velocity and pressure are first governed by the full fluid equations; a steady particle-free solution is then subtracted to isolate the disturbance. This separation provides an exact starting point for the time dependence approximation and regular perturbation model introduced below.

The main background model is the periodic channel–cavity flow, while the inlet–

outlet background is retained as a separate comparison case. The particle disturbance requires its own boundary value specification. The proposed periodic particle formulation represents a sphere at the corresponding position in every repeated cell. It is distinct from a single particle in a periodically structured device, as explained in Section 2.5.4.

For an incompressible Newtonian fluid of constant density ρ and dynamic viscosity μ, the dimensional total velocity $\widehat{\boldsymbol{u}}_{\mathrm{tot}}$ and physical pressure $\widehat{p}_{\mathrm{tot}}$ satisfy the Navier–Stokes equations in the time-dependent fluid domain outside the sphere [22]:

$$\rho\left[\left.\frac{\partial\widehat{\boldsymbol{u}}_{\mathrm{tot}}}{\partial\widehat{t}}\right|_{\widehat{\boldsymbol{x}}}+(\widehat{\boldsymbol{u}}_{\mathrm{tot}}\cdot\widehat{\nabla})\widehat{\boldsymbol{u}}_{\mathrm{tot}}\right]=-\widehat{\nabla}\widehat{p}_{\mathrm{tot}}+\mu\widehat{\nabla}^2\widehat{\boldsymbol{u}}_{\mathrm{tot}}, \tag{2.8}$$

$$\widehat{\nabla}\cdot\widehat{\boldsymbol{u}}_{\mathrm{tot}}=0. \tag{2.9}$$

The derivative is taken at a fixed spatial location in the stationary device; it follows neither the particle nor a fluid element. The no-slip boundary condition requires the fluid velocity to equal the local solid-surface velocity. Thus,

$$\widehat{\boldsymbol{u}}_{\mathrm{tot}}=\boldsymbol{0} \qquad \text{on stationary walls,} \tag{2.10}$$

$$\widehat{\boldsymbol{u}}_{\mathrm{tot}}=\widehat{\boldsymbol{U}}_p+\widehat{\boldsymbol{\Omega}}_p\times(\widehat{\boldsymbol{x}}-\widehat{\boldsymbol{x}}_p) \qquad \text{on the particle surface.} \tag{2.11}$$

For the proposed periodic particle formulation, the total velocity matches on the paired streamwise faces. The physical pressure includes the driving pressure drop; its periodic remainder is distinguished from this drop below.

The fluid exerts force and torque on the sphere through the Newtonian stress [22]

$$\widehat{\boldsymbol{\sigma}}_{\mathrm{tot}}=-\widehat{p}_{\mathrm{tot}}\boldsymbol{I}+\mu\left[\widehat{\nabla}\widehat{\boldsymbol{u}}_{\mathrm{tot}}+(\widehat{\nabla}\widehat{\boldsymbol{u}}_{\mathrm{tot}})^T\right], \tag{2.12}$$

where $\boldsymbol{I}$ is the identity tensor and T denotes transpose [22]. The particle velocities $\widehat{\boldsymbol{U}}_p$ and $\widehat{\boldsymbol{\Omega}}_p$ are therefore coupled to the fluid solution through the force and torque balances in Section 2.5.8.

2.5.3 Background flow and the exact disturbance equation

To separate the effect of the sphere from the background flow, let $\overline{\widehat{\boldsymbol{u}}}$ and $\overline{\widehat{p}}$ denote the steady particle-free solution. This background is defined throughout the empty device, including the volume subsequently occupied by the sphere. Define the velocity and pressure disturbances by

$$\widehat{\boldsymbol{u}}_{\mathrm{tot}}=\overline{\widehat{\boldsymbol{u}}}+\widehat{\boldsymbol{v}}, \qquad \widehat{p}_{\mathrm{tot}}=\overline{\widehat{p}}+\widehat{q}. \tag{2.13}$$

This is a definition, not an assumption that the disturbance is small. The background satisfies the same fluid equations at the same density and viscosity, with no particle present:

$$\left.\frac{\partial \overline{\widehat{\boldsymbol{u}}}}{\partial \widehat{t}}\right|_{\widehat{\boldsymbol{x}}} = \mathbf{0}, \tag{2.14}$$

$$\rho(\overline{\widehat{\boldsymbol{u}}} \cdot \widehat{\nabla})\overline{\widehat{\boldsymbol{u}}} = -\widehat{\nabla}\overline{\widehat{p}} + \mu\widehat{\nabla}^2\overline{\widehat{\boldsymbol{u}}}, \tag{2.15}$$

$$\widehat{\nabla} \cdot \overline{\widehat{\boldsymbol{u}}} = 0. \tag{2.16}$$

Substituting Eq. (2.13) into the total momentum balance gives

$$\begin{aligned}\rho\left[\left.\frac{\partial \widehat{\boldsymbol{v}}}{\partial \widehat{t}}\right|_{\widehat{\boldsymbol{x}}} + \Big((\overline{\widehat{\boldsymbol{u}}} + \widehat{\boldsymbol{v}}) \cdot \widehat{\nabla}\Big)(\overline{\widehat{\boldsymbol{u}}} + \widehat{\boldsymbol{v}})\right] = & -\widehat{\nabla}(\overline{\widehat{p}} + \widehat{q}) \\ & + \mu\widehat{\nabla}^2(\overline{\widehat{\boldsymbol{u}}} + \widehat{\boldsymbol{v}}).\end{aligned} \tag{2.17}$$

Expanding the convective term and subtracting Eq. (2.15) removes the purely background contributions, leaving

$$\rho\left[\left.\frac{\partial \widehat{\boldsymbol{v}}}{\partial \widehat{t}}\right|_{\widehat{\boldsymbol{x}}} + (\overline{\widehat{\boldsymbol{u}}} \cdot \widehat{\nabla})\widehat{\boldsymbol{v}} + (\widehat{\boldsymbol{v}} \cdot \widehat{\nabla})\overline{\widehat{\boldsymbol{u}}} + (\widehat{\boldsymbol{v}} \cdot \widehat{\nabla})\widehat{\boldsymbol{v}}\right] = -\widehat{\nabla}\widehat{q} + \mu\widehat{\nabla}^2\widehat{\boldsymbol{v}}. \tag{2.18}$$

The four surviving terms are local time evolution of the disturbance, transport of the disturbance by the background, interaction of the disturbance with background velocity gradients, and disturbance self advection. The subtraction is exact, and incompressibility similarly gives $\widehat{\nabla} \cdot \widehat{\boldsymbol{v}} = 0$. No time-dependence or inertial term has yet been discarded.

The stress separates just as the velocity and pressure do. For constant viscosity, the Newtonian stress relation in Eq. (2.12) is linear in pressure and velocity gradients. Therefore, $\widehat{\boldsymbol{\sigma}}_{\text{tot}} = \overline{\widehat{\boldsymbol{\sigma}}} + \widehat{\boldsymbol{\sigma}}_v$, where

$$\begin{aligned}\widehat{\boldsymbol{\sigma}}_v &= -\widehat{q}\boldsymbol{I} + \mu\left[\widehat{\nabla}\widehat{\boldsymbol{v}} + (\widehat{\nabla}\widehat{\boldsymbol{v}})^T\right], \\ \widehat{\nabla} \cdot \widehat{\boldsymbol{\sigma}}_v &= -\widehat{\nabla}\widehat{q} + \mu\widehat{\nabla}^2\widehat{\boldsymbol{v}}.\end{aligned} \tag{2.19}$$

The second identity uses constant viscosity and $\widehat{\nabla} \cdot \widehat{\boldsymbol{v}} = 0$. Thus, the disturbance stress is obtained by subtracting the background stress from the total stress; no additional assumption about the fluid's stress response is introduced.

2.5.4 Disturbance boundary conditions and particle domain choice

Subtracting the background velocity from the physical surface conditions determines the disturbance boundary values:

$$\widehat{\boldsymbol{v}} = \widehat{\boldsymbol{U}}_p + \widehat{\boldsymbol{\Omega}}_p \times (\widehat{\boldsymbol{x}} - \widehat{\boldsymbol{x}}_p) - \overline{\widehat{\boldsymbol{u}}}(\widehat{\boldsymbol{x}}) \qquad \text{on the particle,} \tag{2.20}$$

$$\widehat{\boldsymbol{v}} = \boldsymbol{0} \qquad \text{on stationary walls.} \tag{2.21}$$

On the surface of the finite-sized sphere, the background is evaluated at each surface point. The disturbance supplies the correction needed to enforce rigid motion, including all three components of the background velocity.

Periodicity of the particle-free background does not by itself prescribe periodicity of the particle disturbance. The periodic particle formulation considered here represents a sphere at the corresponding position in every repeated cell. This is distinct from a single-particle formulation in a periodically structured device. Hasimoto [23, p. 318, Eq. (2.1); p. 321, Sec. 4] provides a classical Stokes-flow treatment of periodic sphere arrays. That work is a precedent for the periodic-array interpretation, not a solution of the present wall-bounded, streamwise-periodic cavity problem. The disturbance boundary model will therefore be identified separately from the background-flow boundary conditions for every reported calculation.

For the proposed periodic particle formulation, the total velocity is required to match on the paired streamwise faces, following the standard streamwise-periodic matching condition [24, p. 182, Eq. (12)].

Since the background velocity has the same period, subtraction gives

$$\widehat{\boldsymbol{v}}(\widehat{\boldsymbol{x}} + \widehat{\boldsymbol{\ell}}, \widehat{t}) = \widehat{\boldsymbol{v}}(\widehat{\boldsymbol{x}}, \widehat{t}) \qquad \text{on paired faces,} \tag{2.22}$$

where $\widehat{\boldsymbol{\ell}} = \widehat{L}_p \boldsymbol{e}_x$ is the period vector. This condition matches disturbance values across the paired faces rather than prescribing them to be zero. In the present model, the particle-containing cell is repeated periodically; an isolated-particle far-field condition is therefore not imposed, and this is our boundary model choice.

A separate finite-end disturbance model may instead prescribe

$$\widehat{\boldsymbol{v}} = \boldsymbol{0} \quad \Longrightarrow \quad \widehat{\boldsymbol{u}}_{\mathrm{tot}} = \overline{\widehat{\boldsymbol{u}}} \qquad \text{on the computational end planes.} \tag{2.23}$$

This imposes the background velocity at the end planes, rather than imposing the total-flow no-slip condition; the total end velocity vanishes only where the background velocity vanishes. When used to approximate an isolated particle, zero disturbance

at finite ends is a truncation approximation whose adequacy requires a domain-size assessment. It is a different boundary value problem and is not used interchangeably with the periodic formulation below. Once the periodic particle domain model has been specified, its driving condition must also be selected. Following the streamwise-periodic pressure decomposition of Patankar *et al.* [24, p. 182, Eqs. (5)–(6)], we write the physical pressure as a periodic remainder plus a linear streamwise drop. Let $\widehat{g}$ be the background pressure-gradient magnitude and let $\delta\widehat{g}(\widehat{t})$ be its change when the particle is present:

$$\overline{\widehat{p}} = \overline{\widehat{p}}_{\mathrm{per}} - \widehat{g}\,\widehat{x}, \tag{2.24}$$

$$\widehat{p}_{\mathrm{tot}} = \widehat{p}_{\mathrm{tot,per}} - (\widehat{g} + \delta\widehat{g}(\widehat{t}))\widehat{x}, \tag{2.25}$$

$$\widehat{q} = \widehat{q}_{\mathrm{per}} - \delta\widehat{g}(\widehat{t})\widehat{x}, \qquad -\widehat{\nabla}\widehat{q} = -\widehat{\nabla}\widehat{q}_{\mathrm{per}} + \delta\widehat{g}(\widehat{t})\boldsymbol{e}_x. \tag{2.26}$$

Here $\widehat{q}_{\mathrm{per}} = \widehat{p}_{\mathrm{tot,per}} - \overline{\widehat{p}}_{\mathrm{per}}$. The pressure remainders are periodic; their time arguments are omitted for brevity. The driving may prescribe either the pressure drop or the flow rate [25].

At fixed imposed pressure gradient, $\delta\widehat{g} = 0$ and $\widehat{q}$ is periodic, while the flow rate may change. Alternatively, fixing the total flux to its background value makes $\delta\widehat{g}(\widehat{t})$ an additional unknown. Since $\widehat{\boldsymbol{u}}_{\mathrm{tot}} = \overline{\widehat{\boldsymbol{u}}} + \widehat{\boldsymbol{v}}$, equality of the total and background fluxes requires

$$\int_{\widehat{\Gamma}_b} \widehat{v}_x \,\mathrm{d}\widehat{A} = 0, \tag{2.27}$$

where $\widehat{\Gamma}_b$ is a complete straight-channel cross section that does not intersect the particle at the configuration considered. This constraint permits a change in velocity profile but not in its integrated flux.

Fixed pressure gradient and fixed flux define alternative periodic particle-containing problems. The proposed free-particle calculation uses fixed imposed pressure gradient, as specified in Section 3.6.4. Thus $\delta\widehat{g} = 0$, $\widehat{q}$ is periodic, and Eq. (2.27) is not imposed. This is an explicit modelling choice, separate from the reference velocity and from the periodicity of the particle-free background. Together, the surface conditions, particle-domain model and driving condition specify the boundary and forcing conditions for the disturbance equations. The particle motion is determined through the balances in Section 2.5.8.

2.5.5 Laboratory time dependence

Even with a steady background, the disturbance generally changes at a fixed device location as the sphere moves. The treatment of this evolution is not yet finalised. One approach is to neglect evolution in particle-translating coordinates while retaining

the corresponding laboratory-frame transport term. The equations below describe that approach, whose accuracy will be assessed before it is used for physical particle predictions.

To distinguish transport of the disturbance from changes in its shape, we introduce coordinates that translate with the particle but do not rotate:

$$\widehat{\boldsymbol{r}} = \widehat{\boldsymbol{x}} - \widehat{\boldsymbol{x}}_p(\widehat{t}), \qquad \widehat{\boldsymbol{V}}(\widehat{\boldsymbol{r}}, \widehat{t}) = \widehat{\boldsymbol{v}}(\widehat{\boldsymbol{r}} + \widehat{\boldsymbol{x}}_p(\widehat{t}), \widehat{t}). \tag{2.28}$$

Here $\widehat{\boldsymbol{V}}$ is the same disturbance expressed using a different position coordinate; it is not obtained by subtracting the particle velocity. Using $\mathrm{d}\widehat{\boldsymbol{x}}_p/\mathrm{d}\widehat{t} = \widehat{\boldsymbol{U}}_p$, the chain rule gives the exact identity

$$\left.\frac{\partial \widehat{\boldsymbol{v}}}{\partial \widehat{t}}\right|_{\widehat{\boldsymbol{x}}} = \left.\frac{\partial \widehat{\boldsymbol{V}}}{\partial \widehat{t}}\right|_{\widehat{\boldsymbol{r}}} - (\widehat{\boldsymbol{U}}_p \cdot \nabla_{\widehat{\boldsymbol{r}}})\widehat{\boldsymbol{V}}. \tag{2.29}$$

This identity is the rigid-translation special case of the standard time-derivative transformation under a moving coordinate map [26]. The first term describes evolution seen while following the sphere; the second describes translation of the disturbance past a fixed spatial location.

The transported-disturbance approximation retains the second contribution and neglects the first:

$$\left.\frac{\partial \widehat{\boldsymbol{V}}}{\partial \widehat{t}}\right|_{\widehat{\boldsymbol{r}}} \approx \boldsymbol{0}, \qquad \left.\frac{\partial \widehat{\boldsymbol{v}}}{\partial \widehat{t}}\right|_{\widehat{\boldsymbol{x}}} \approx -(\widehat{\boldsymbol{U}}_p \cdot \widehat{\nabla})\widehat{\boldsymbol{v}}. \tag{2.30}$$

Changing coordinates is exact; neglecting evolution in translating coordinates is the modelling assumption. It omits changes in disturbance shape and amplitude associated with motion through a spatially varying background, changing wall proximity, and changes in the particle's translational or angular velocity. A related travelling-wave assumption is used in the moving-singularity model of Christensen and Roper [9]. That work motivates the comparison but does not establish the validity of the present resolved-sphere approximation in a cavity.

Substituting Eq. (2.30) into the exact disturbance equation yields

$$\rho\Big[((\overline{\widehat{\boldsymbol{u}}} - \widehat{\boldsymbol{U}}_p) \cdot \widehat{\nabla})\widehat{\boldsymbol{v}} + (\widehat{\boldsymbol{v}} \cdot \widehat{\nabla})\overline{\widehat{\boldsymbol{u}}} + (\widehat{\boldsymbol{v}} \cdot \widehat{\nabla})\widehat{\boldsymbol{v}}\Big] \approx -\widehat{\nabla}\widehat{q} + \mu\widehat{\nabla}^2\widehat{\boldsymbol{v}}. \tag{2.31}$$

Equivalently, the inertial expression is $((\overline{\widehat{\boldsymbol{u}}} + \widehat{\boldsymbol{v}} - \widehat{\boldsymbol{U}}_p) \cdot \widehat{\nabla})\widehat{\boldsymbol{v}} + (\widehat{\boldsymbol{v}} \cdot \widehat{\nabla})\overline{\widehat{\boldsymbol{u}}}$. It combines transport of the disturbance by the total velocity relative to the sphere with interaction between the disturbance and background velocity gradients.

The approximation acts on the disturbance after the background equation has been subtracted. It therefore introduces no extra term $-(\widehat{\boldsymbol{U}}_p \cdot \widehat{\nabla})\overline{\widehat{\boldsymbol{u}}}$. Its absence follows from the derivation, not from an assumption that the background is spatially uniform.

The omitted contribution is $\rho\,\partial\widehat{\boldsymbol{V}}/\partial\widehat{t}|_{\widehat{\boldsymbol{r}}}$. Its importance must be assessed independently of the particle Reynolds number: a small inertial contribution to the total flow does not ensure that one part of that contribution is negligible relative to the other parts. Where this omission is not justified, disturbance evolution must be retained or the closure revised.

Equation (2.31) still retains nonlinear disturbance inertia. The separate perturbation approximation is introduced after the scales have been fixed.

2.5.6 Mean velocity nondimensionalisation

A common reference scale is needed to compare the background driving conditions and to express the particle response consistently. Length is scaled by the vertical cavity depth $\widehat{H}_c$, and velocity by the target upstream cross sectional mean $\widehat{U}_{\mathrm{ref}} = \widehat{U}_{b,\mathrm{target}}$. Thus,

$$\begin{aligned} \boldsymbol{x} &= \frac{\widehat{\boldsymbol{x}}}{\widehat{H}_c}, \qquad t = \frac{\widehat{U}_{\mathrm{ref}}\widehat{t}}{\widehat{H}_c}, \qquad \boldsymbol{u}_{\mathrm{tot}} = \frac{\widehat{\boldsymbol{u}}_{\mathrm{tot}}}{\widehat{U}_{\mathrm{ref}}}, \\ \overline{\boldsymbol{u}} &= \frac{\overline{\widehat{\boldsymbol{u}}}}{\widehat{U}_{\mathrm{ref}}}, \qquad \boldsymbol{v} = \frac{\widehat{\boldsymbol{v}}}{\widehat{U}_{\mathrm{ref}}}, \qquad q = \frac{\widehat{H}_c\widehat{q}}{\mu\widehat{U}_{\mathrm{ref}}}. \end{aligned} \tag{2.32}$$

Total and background pressures use the same viscous pressure scale $\mu\widehat{U}_{\mathrm{ref}}/\widehat{H}_c$ and a common arbitrary reference pressure $\widehat{p}_{\mathrm{ref}}$, so their difference is q. Particle translation uses the same velocity scale, while angular velocity is scaled by $\widehat{U}_{\mathrm{ref}}/\widehat{H}_c$. The reference velocity is fixed by the background normalisation: choosing these units does not impose fixed flux on the fluid containing a particle problem. The corresponding mean-based Reynolds number is

$$\mathrm{Re} = \frac{\rho\widehat{U}_{\mathrm{ref}}\widehat{H}_c}{\mu}. \tag{2.33}$$

For the inlet–outlet background, the dimensionless equations are

$$\mathrm{Re}(\overline{\boldsymbol{u}}\cdot\nabla)\overline{\boldsymbol{u}} = -\nabla\overline{p} + \nabla^2\overline{\boldsymbol{u}}, \tag{2.34}$$

$$\nabla\cdot\overline{\boldsymbol{u}} = 0. \tag{2.35}$$

For the periodic background, the decomposition $\overline{p} = \overline{p}_{\mathrm{per}} - gx$ instead gives

$$\mathrm{Re}(\overline{\boldsymbol{u}}\cdot\nabla)\overline{\boldsymbol{u}} = -\nabla\overline{p}_{\mathrm{per}} + \nabla^2\overline{\boldsymbol{u}} + g\boldsymbol{e}_x, \qquad g = \frac{\widehat{g}\widehat{H}_c^2}{\mu\widehat{U}_{\mathrm{ref}}}. \tag{2.36}$$

The periodic velocity and pressure remainder match across the paired faces. In background calculations labelled $\mathrm{Re} = 0$, the inertial term is omitted while non-zero unit-mean flow is retained; this is the normalised Stokes reference problem. For the inlet–outlet comparison, the principal inlet profile is the mean-normalised rectangular-

duct Poiseuille solution. Fully developed axial flow in a straight duct is determined by a cross sectional Poisson problem with no slip [27]. Accordingly, let $\widetilde{u}_P$ solve $\nabla_\perp^2 \widetilde{u}_P = -K$, with $K > 0$ constant and $\widetilde{u}_P = 0$ on the rectangular boundary, and define

$$u_P(y,z) = \frac{\widetilde{u}_P(y,z)}{\widetilde{U}_{P,b}}, \qquad \widetilde{U}_{P,b} = \frac{1}{HW}\int_{-W/2}^{W/2}\int_0^H \widetilde{u}_P(y,z)\,\mathrm{d}y\,\mathrm{d}z. \tag{2.37}$$

The arbitrary amplitude K cancels in this normalisation. A second inlet profile is retained solely as a sensitivity case:

$$u_Q(y,z) = 9\frac{y}{H}\left(1-\frac{y}{H}\right)\left[1-\left(\frac{2z}{W}\right)^2\right]. \tag{2.38}$$

Both prescribe $\overline{\boldsymbol{u}} = u_{P,Q}\boldsymbol{e}_x$ with unit cross sectional mean. The quadratic product satisfies the side-boundary values and mean constraint, but is not the fully developed rectangular-duct solution. These are background inlet specifications, not replacements for the periodic particle boundary conditions above.

Using the same device scales, the exact disturbance equation becomes

$$\mathrm{Re}\left[\left.\frac{\partial \boldsymbol{v}}{\partial t}\right|_{\boldsymbol{x}} + (\overline{\boldsymbol{u}}\cdot\nabla)\boldsymbol{v} + (\boldsymbol{v}\cdot\nabla)\overline{\boldsymbol{u}} + (\boldsymbol{v}\cdot\nabla)\boldsymbol{v}\right] = -\nabla q + \nabla^2\boldsymbol{v}, \qquad \nabla\cdot\boldsymbol{v} = 0. \tag{2.39}$$

Here q is the full disturbance pressure, including any linear correction:

$$q = q_{\mathrm{per}} - \delta g(t)x, \qquad \delta g(t) = \frac{\delta\widehat{g}(\widehat{t})\widehat{H}_c^2}{\mu\widehat{U}_{\mathrm{ref}}}. \tag{2.40}$$

Consequently, solving for q_{per} rather than q replaces the right-hand side of Eq. (2.39) by $-\nabla q_{\mathrm{per}} + \nabla^2\boldsymbol{v} + \delta g(t)\boldsymbol{e}_x$. The pressure-gradient correction is represented in one of these two ways, not in both simultaneously.

2.5.7 Particle scales and regular perturbation

The device Reynolds number measures inertia on the cavity scale, whereas the proposed disturbance expansion is organised on the particle scale. Introduce the reference shear rate $\widehat{G} = \widehat{U}_{\mathrm{ref}}/\widehat{H}_c$ and the dimensional particle scales

$$\begin{gathered} \kappa = \frac{\widehat{a}}{\widehat{H}_c}, \qquad \widehat{\ell}_s = \widehat{a}, \qquad \widehat{U}_s = \widehat{G}\widehat{a} = \kappa\widehat{U}_{\mathrm{ref}}, \\ \widehat{t}_s = \frac{\widehat{\ell}_s}{\widehat{U}_s} = \frac{\widehat{H}_c}{\widehat{U}_{\mathrm{ref}}}, \qquad \widehat{p}_s = \frac{\mu\widehat{U}_s}{\widehat{\ell}_s}, \qquad \mathrm{Re}_p = \frac{\rho\widehat{U}_s\widehat{\ell}_s}{\mu} = \kappa^2\mathrm{Re}. \end{gathered} \tag{2.41}$$

This uses the particle radius and a shear-based disturbance speed. It is the same type of scaling used by Hood *et al.* [6], but with the present cross sectional mean velocity

and cavity depth instead of their centreline velocity and channel width. The reference $\widehat{G}$ is a scale, not a measurement of local cavity shear, so Re_p alone does not quantify every local inertial effect.

A subscript s denotes quantities expressed in particle units. Their relation to the device variables is

$$\begin{gathered}\boldsymbol{r}_s = \frac{\boldsymbol{x}-\boldsymbol{x}_p}{\kappa}, \qquad \boldsymbol{v}_s = \frac{\boldsymbol{v}}{\kappa}, \qquad \boldsymbol{U}_{p,s} = \frac{\boldsymbol{U}_p}{\kappa}, \\ q_s = q, \qquad \nabla_s = \kappa\nabla.\end{gathered} \tag{2.42}$$

Time, angular velocity and pressure have the same scales in the two systems. The equations below are nevertheless written in device units, so the factor Re cannot simply be replaced by Re_p.

The reduction is a formal expansion of disturbance inertia at a fixed particle configuration and a prescribed background. More precisely, one may replace its device-scale coefficient Re by ϵ/κ^2, expand in ϵ while holding κ and the background fixed, and finally set $\epsilon = \mathrm{Re}_p$. After that identification:

$$\boldsymbol{v} = \boldsymbol{v}_0 + \mathrm{Re}_p\boldsymbol{v}_1 + O(\mathrm{Re}_p^2), \tag{2.43}$$

$$q = q_0 + \mathrm{Re}_p q_1 + O(\mathrm{Re}_p^2), \tag{2.44}$$

$$\boldsymbol{u}_{\mathrm{tot}} = \overline{\boldsymbol{u}} + \boldsymbol{v}_0 + \mathrm{Re}_p\boldsymbol{v}_1 + O(\mathrm{Re}_p^2). \tag{2.45}$$

The finite-Re background is retained rather than expanded. Thus this is not an asymptotic expansion of the entire coupled background–particle problem. The displayed remainder is formal, and uniform validity as κ varies has not been established for the cavity. Hood *et al.* [6] provide a precedent for a regular disturbance expansion in straight-channel Poiseuille flow, not a validation of this frozen-background cavity construction.

The particle motion has a corresponding expansion,

$$\begin{aligned}\boldsymbol{U}_p &= \boldsymbol{U}_0 + \mathrm{Re}_p\boldsymbol{U}_1 + O(\mathrm{Re}_p^2), \\ \boldsymbol{\Omega}_p &= \boldsymbol{\Omega}_0 + \mathrm{Re}_p\boldsymbol{\Omega}_1 + O(\mathrm{Re}_p^2).\end{aligned} \tag{2.46}$$

Under the assumed viscous leading balance, the leading disturbance solves

$$-\nabla q_0 + \nabla^2\boldsymbol{v}_0 = \boldsymbol{0}, \qquad \nabla\cdot\boldsymbol{v}_0 = 0, \tag{2.47}$$

with, for $\boldsymbol{r} = \boldsymbol{x} - \boldsymbol{x}_p$,

$$\boldsymbol{v}_0 = \boldsymbol{U}_0 + \boldsymbol{\Omega}_0\times\boldsymbol{r} - \overline{\boldsymbol{u}}(\boldsymbol{x}) \qquad \text{on the particle.} \tag{2.48}$$

No slip on the walls and periodic matching apply order by order. The driving constraint must also be retained at each order. In a fixed-flux calculation,

$$q_j = q_{j,\mathrm{per}} - \delta g_j x, \qquad \int_{\Gamma_b} (\boldsymbol{v}_j)_x \,\mathrm{d}A = 0, \qquad j = 0, 1, \tag{2.49}$$

where $\delta g = \delta g_0 + \mathrm{Re}_p \delta g_1 + O(\mathrm{Re}_p^2)$. The leading correction δg_0 need not vanish: the sphere can change the pressure gradient needed to maintain flux even in the leading Stokes problem. At fixed pressure gradient, instead, $\delta g_0 = \delta g_1 = 0$, and these flux constraints are not imposed. Because the background variation is imposed over the resolved sphere surface, no additional point-particle Faxén curvature term is added to this leading boundary value problem.

The first inertial source is obtained by evaluating the retained inertial terms on the leading solution. Before imposing a disturbance-time closure, its general laboratory-frame form is

$$\begin{aligned} \boldsymbol{N}_0^{\mathrm{gen}} = & \left.\frac{\partial \boldsymbol{v}_0}{\partial t}\right|_{\boldsymbol{x}} + (\overline{\boldsymbol{u}} \cdot \nabla)\boldsymbol{v}_0 \\ & + (\boldsymbol{v}_0 \cdot \nabla)\overline{\boldsymbol{u}} + (\boldsymbol{v}_0 \cdot \nabla)\boldsymbol{v}_0. \end{aligned} \tag{2.50}$$

The laboratory time derivative must be evaluated consistently with the leading particle motion and the dependence of the disturbance on particle configuration.

Under the candidate transported-disturbance closure,

$$\left.\frac{\partial \boldsymbol{v}_0}{\partial t}\right|_{\boldsymbol{x}} \approx -(\boldsymbol{U}_0 \cdot \nabla)\boldsymbol{v}_0.$$

The general source is then approximated by the specialised source $\boldsymbol{N}_0$:

$$\begin{aligned} \boldsymbol{N}_0 = & ((\overline{\boldsymbol{u}} - \boldsymbol{U}_0) \cdot \nabla)\boldsymbol{v}_0 + (\boldsymbol{v}_0 \cdot \nabla)\overline{\boldsymbol{u}} \\ & + (\boldsymbol{v}_0 \cdot \nabla)\boldsymbol{v}_0. \end{aligned} \tag{2.51}$$

Equations (2.50) and (2.51) distinguish the unclosed laboratory-frame source from the expression obtained under the candidate approximation.

Using $\mathrm{Re} = \mathrm{Re}_p/\kappa^2$, formal coefficient matching with this specialised source gives

$$-\nabla q_1 + \nabla^2 \boldsymbol{v}_1 = \kappa^{-2} \boldsymbol{N}_0, \qquad \nabla \cdot \boldsymbol{v}_1 = 0, \tag{2.52}$$

$$\boldsymbol{v}_1 = \boldsymbol{U}_1 + \boldsymbol{\Omega}_1 \times \boldsymbol{r} \qquad \text{on the particle.} \tag{2.53}$$

Here $\boldsymbol{v}_1 = \boldsymbol{0}$ on stationary walls and matches periodically across the paired faces for the proposed periodic particle model, with the pressure convention and driving constraint chosen above.

Without the transported-disturbance approximation, the source also contains $\partial \boldsymbol{V}_0/\partial t|_{\boldsymbol{r}}$, evaluated at the corresponding point, where $\boldsymbol{V}_0$ is the leading disturbance in translating coordinates. In that case, $\boldsymbol{N}_0^{\mathrm{gen}}$ replaces $\boldsymbol{N}_0$ in the correction equation. Neglect of this contribution is a closure assumption, not a consequence of coefficient matching.

It is useful to distinguish the coefficient $\boldsymbol{v}_1$ from the actual first fluid increment $\delta\boldsymbol{v} = \mathrm{Re}_p \boldsymbol{v}_1$. With $\delta q = \mathrm{Re}_p q_1$, the latter satisfies

$$-\nabla \delta q + \nabla^2 \delta \boldsymbol{v} = \mathrm{Re}\boldsymbol{N}_0, \qquad \nabla \cdot \delta \boldsymbol{v} = 0. \tag{2.54}$$

This equation uses the same candidate closure as Eq. (2.52); retaining disturbance evolution requires the corresponding general source in both representations.

Neither $\boldsymbol{v}_1$ nor $\delta\boldsymbol{v}$ is a particle lift force or migration velocity. The incremental inertial particle velocity is $\mathrm{Re}_p \boldsymbol{U}_1$, determined together with $\mathrm{Re}_p \boldsymbol{\Omega}_1$ from the load balances below. Even the leading velocity $\boldsymbol{U}_0$ need not equal $\overline{\boldsymbol{u}}(\boldsymbol{x}_p)$, because finite size and the walls are already present in the leading boundary value problem. Assessment of the reduction must therefore consider local slip, background gradients, wall clearance, disturbance evolution and the size of the computed correction, rather than Re_p alone.

2.5.8 Hydrodynamic loads and particle motion

The disturbance problems determine the fluid response for a specified rigid motion. The remaining step is to determine that motion from the loads exerted on the particle. Using the total stress in Eq. (2.12), and taking $\boldsymbol{n}_p$ outward from the particle into the fluid, the hydrodynamic force and torque are the surface traction integrals [22, §1.3, pp. 9–11]:

$$\widehat{\boldsymbol{F}}_H = \int_{\widehat{S}_p} \widehat{\boldsymbol{\sigma}}_{\mathrm{tot}} \boldsymbol{n}_p \, \mathrm{d}\widehat{S}, \tag{2.55}$$

$$\widehat{\boldsymbol{T}}_H = \int_{\widehat{S}_p} (\widehat{\boldsymbol{x}} - \widehat{\boldsymbol{x}}_p) \times (\widehat{\boldsymbol{\sigma}}_{\mathrm{tot}} \boldsymbol{n}_p) \, \mathrm{d}\widehat{S}. \tag{2.56}$$

On the same surface, the outward normal of the fluid domain is $-\boldsymbol{n}_p$. This distinction fixes the sign when surface loads are compared with weak reactions.

For a homogeneous rigid sphere, Newton's translational and rotational balances are

$$m_p \frac{\mathrm{d}\widehat{\boldsymbol{U}}_p}{\mathrm{d}\widehat{t}} = \widehat{\boldsymbol{F}}_H + \widehat{\boldsymbol{F}}_{\mathrm{ext}}, \tag{2.57}$$

$$I_p \frac{\mathrm{d}\widehat{\boldsymbol{\Omega}}_p}{\mathrm{d}\widehat{t}} = \widehat{\boldsymbol{T}}_H + \widehat{\boldsymbol{T}}_{\mathrm{ext}}, \qquad m_p = \frac{4\pi}{3}\rho_p \widehat{a}^3, \quad I_p = \frac{2}{5} m_p \widehat{a}^2. \tag{2.58}$$

The terms with subscript ext represent externally imposed loads. Neutral buoyancy

means $\rho_p = \rho$; it does not set the particle acceleration to zero.

Importantly, subtracting the background momentum equation does not remove background stress from the particle load. Since $\widehat{\boldsymbol{\sigma}}_{\mathrm{tot}} = \overline{\widehat{\boldsymbol{\sigma}}} + \widehat{\boldsymbol{\sigma}}_v$, both contributions enter the surface integrals. The background is smooth through the sphere volume $\widehat{B}_p$, so the divergence theorem and Eq. (2.15) give

$$\begin{aligned} \widehat{\boldsymbol{F}}_{\mathrm{bg}} &= \int_{\widehat{S}_p} \overline{\widehat{\boldsymbol{\sigma}}} \boldsymbol{n}_p \, \mathrm{d}\widehat{S} \\ &= \rho \int_{\widehat{B}_p} (\overline{\widehat{\boldsymbol{u}}} \cdot \widehat{\nabla}) \overline{\widehat{\boldsymbol{u}}} \, \mathrm{d}\widehat{V}. \end{aligned} \tag{2.59}$$

Because the Newtonian stress is symmetric [22, §1.3, p. 11], the corresponding background torque can likewise be written as

$$\begin{aligned} \widehat{\boldsymbol{T}}_{\mathrm{bg}} &= \int_{\widehat{S}_p} (\widehat{\boldsymbol{x}} - \widehat{\boldsymbol{x}}_p) \times \left(\overline{\widehat{\boldsymbol{\sigma}}} \boldsymbol{n}_p \right) \mathrm{d}\widehat{S} \\ &= \rho \int_{\widehat{B}_p} (\widehat{\boldsymbol{x}} - \widehat{\boldsymbol{x}}_p) \times \left[(\overline{\widehat{\boldsymbol{u}}} \cdot \widehat{\nabla}) \overline{\widehat{\boldsymbol{u}}} \right] \mathrm{d}\widehat{V}. \end{aligned} \tag{2.60}$$

Neither background contribution is assumed to vanish in the cavity. The surface loads must also retain any linear pressure correction in the physical pressure; using the periodic remainder alone would omit its contribution.

To combine these balances with the device-scaled fluid fields, define $\beta = \rho_p/\rho$, $V_\kappa = 4\pi\kappa^3/3$ and $J_\kappa = 8\pi\kappa^5/15$. Scaling force by $\mu \widehat{U}_{\mathrm{ref}} \widehat{H}_c$ and torque by $\mu \widehat{U}_{\mathrm{ref}} \widehat{H}_c^2$ gives

$$\beta \mathrm{Re} V_\kappa \frac{\mathrm{d}\boldsymbol{U}_p}{\mathrm{d}t} = \boldsymbol{F}_H + \boldsymbol{F}_{\mathrm{ext}}, \tag{2.61}$$

$$\beta \mathrm{Re} J_\kappa \frac{\mathrm{d}\boldsymbol{\Omega}_p}{\mathrm{d}t} = \boldsymbol{T}_H + \boldsymbol{T}_{\mathrm{ext}}. \tag{2.62}$$

These are the total balances to which the reduced disturbance solution must be matched.

For the proposed leading unforced Stokes resistance calculation, the disturbance force and torque are set to zero under an ordering that assigns background loads and particle inertia to the correction. This is an additional assumption of the reduction, not a consequence of neutral buoyancy. This load ordering must be made consistent with the same formal parameter used in the disturbance expansion; it does not follow from holding the finite-Re background fixed. At first order, the disturbance correction, background stress and particle acceleration must be combined consistently in the total balances. If the leading translational and angular velocities are instantaneous maps $\boldsymbol{U}_0(\boldsymbol{x}_p)$ and $\boldsymbol{\Omega}_0(\boldsymbol{x}_p)$ at fixed model parameters, then along the leading trajectory

$$\frac{\mathrm{d}\boldsymbol{U}_0}{\mathrm{d}t} = (\boldsymbol{U}_0 \cdot \nabla_{\boldsymbol{x}_p}) \boldsymbol{U}_0, \qquad \frac{\mathrm{d}\boldsymbol{\Omega}_0}{\mathrm{d}t} = (\boldsymbol{U}_0 \cdot \nabla_{\boldsymbol{x}_p}) \boldsymbol{\Omega}_0. \tag{2.63}$$

The derivatives act on the position-dependent particle-response maps, not directly on the background velocity field. A steady background therefore does not make these accelerations vanish.

Together, the fluid boundary value problems and particle balances define the proposed route from the verified background flow to translation, rotation and trajectories. The exact background subtraction and coordinate transformation are distinct from the three approximation steps: neglect of disturbance evolution in translating coordinates, the regular disturbance expansion, and the ordering used for the particle loads. Their consistency and accuracy in the cavity remain to be assessed through the numerical solution and verification.

Chapter 3

Methodology

3.1 Computational geometry and particle meshes

The calculations use the full 3D geometry defined in Section 2.5.1 and shown in Fig. 2.1. The particle-free background mesh covers the complete channel–cavity domain. For a particle calculation, the spherical region is removed from the fluid domain and a mesh fitted to the particle boundary is generated.

The particle-fitted meshes are generated using Gmsh [28]. The background-flow mesh and the particle-fitted mesh are separate numerical objects. Particle-mesh refinement is controlled by a target characteristic element size h_p near the sphere, a target bulk size h_b, and the spatial transition between them. Both sizes are expressed in units of the cavity depth $\widehat{H}_c$. They do not denote the numbers of background-mesh points in the coordinate directions.

The matching saved background field is loaded and transferred before the background-driven Stokes problem and the combined leading-motion calculation. The mesh-only stage and the rigid-motion resistance problems, including the initial unit-translation test, do not require background velocity data. The leading background problem requires the background velocity on the particle surface, while the subsequent inertial volume integrals require background values and spatial derivatives throughout their integration domain.

3.2 Flow normalisation and flux verification

All flow cases use the mean-velocity convention in Section 2.5.6. On a fixed, complete straight-channel section Γ_b, the achieved background flux and mean velocity are

$$Q = \int_{\Gamma_b} \overline{u}_x \, \mathrm{d}A, \qquad U_b = \frac{Q}{A_{\mathrm{ch}}} = \frac{\widehat{U}_{b,\mathrm{achieved}}}{\widehat{U}_{\mathrm{ref}}}. \tag{3.1}$$

The integral uses the signed streamwise component, not the velocity magnitude. The common targets are

$$U_{b,\mathrm{target}} = 1, \qquad Q_{\mathrm{target}} = A_{\mathrm{ch}} U_{b,\mathrm{target}} = \frac{17}{16} = 1.0625. \tag{3.2}$$

Achieved values are independently integrated from each saved field and compared with these targets. Achieving $U_b = 1$ within tolerance is therefore a verification result, rather than an automatic consequence of scaling.

3.3 Boundary condition and forcing implementation

The periodic background problem uses Eq. (2.36), no slip on stationary walls, and matching velocity and pressure-remainder values on the paired streamwise faces. The pressure null mode is removed by the recorded solver constraint. The driving magnitude g is iterated until

$$|U_b - 1| < \varepsilon_b, \qquad \varepsilon_b = 10^{-4}, \tag{3.3}$$

The inlet–outlet reference uses the mean-normalised rectangular-duct profile in Eq. (2.37). The ten-mode implementation has continuum mean one and diagnostic inlet maximum $U_{P,\mathrm{in,max}} \simeq 1.75658574$. The secondary quadratic profile in Eq. (2.38) has mean one and maximum 9/4. These maxima characterise profile shape and do not define Reynolds number. For reproducibility, the outlet condition and pressure constraint must also be recorded for each inlet–outlet calculation.

For particle calculations, the implementation must first identify the disturbance boundary model independently of the background-flow boundary conditions. A periodic background cache does not by itself implement periodic particle constraints. The finite-end reference adaptation and a periodic-particle implementation represent different boundary value problems and must be identified separately in the calculation record.

For the proposed periodic particle formulation, the implementation must also identify whether the imposed pressure gradient or total flux is held fixed, as defined in Section 2.5.4. The proposed main-channel free-particle calculation uses the fixed-gradient formulation. A fixed-flux calculation would instead require the additional pressure-gradient unknown and flux constraint; periodic velocity matching alone does not impose that constraint.

3.4 Background-flow discretisation and verification

The background-flow equations are solved using DOLFINx within the FEniCSx framework. The production discretisation uses continuous quadratic velocity and continuous

linear pressure elements, forming the Taylor–Hood P_2/P_1 pair on the full 3D geometry. Newton linearisation is used to solve the steady nonlinear problem. At each Newton iteration, the resulting linear saddle-point system is solved by direct LU factorisation through PETSc using MUMPS in the serial reference implementation.

3.5 Background-flow topology analysis

Throughout this section, (u, v, w) denote the components of the steady background velocity $\overline{\boldsymbol{u}}$. At a retained depth $z = z_i$, the reduced in-plane field is

$$\boldsymbol{u}_\perp = (u, v). \tag{3.4}$$

Its interior critical points satisfy

$$u(x^*, y^*, z_i) = 0, \qquad v(x^*, y^*, z_i) = 0. \tag{3.5}$$

Roots on no-slip walls are excluded. An in-plane critical point is a full 3D stagnation point only when $w = 0$ as well.

A consistently selected branch of accepted roots is continued across adjacent depths to define the principal centre-track

$$\Gamma_c = \{(x^*(z), y^*(z), z) : z \in \mathcal{I}_c\}, \tag{3.6}$$

where $\mathcal{I}_c$ is the depth interval over which the branch is continuously resolved. The branch-selection rule, any root degeneracy, and any loss of continuation are recorded. The centre-track is a geometric locus of fixed-depth critical points; it does not generally coincide with a fluid streamline or particle trajectory. The term "centre-track" does not imply that every retained root is a centre in the dynamical-systems sense.

The depthwise velocity and the local in-plane Jacobian evaluated on the track are

$$w^*(z) = w(x^*(z), y^*(z), z), \qquad J_\perp(z) = \begin{pmatrix} u_x & u_y \\ v_x & v_y \end{pmatrix}_{(x^*(z), y^*(z), z)}. \tag{3.7}$$

When $J_\perp$ has the complex-conjugate eigenvalues

$$\lambda_{1,2} = \alpha \pm i|\beta|, \qquad |\beta| > 0, \tag{3.8}$$

$\alpha < 0$ identifies a locally attracting spiral and $\alpha > 0$ a locally repelling spiral of the reduced fixed-depth field. When $\alpha = 0$, linearisation alone does not determine nonlinear stability [18]. Where $w \neq 0$, fluid trajectories leave the retained slice, so this

classification does not by itself describe the full 3D motion.

The near-midplane depthwise diagnostic is

$$\gamma_{\text{track}} = \left.\frac{\mathrm{d}w^*}{\mathrm{d}z}\right|_{z=0}. \tag{3.9}$$

For a differentiable root branch, the chain rule gives

$$\frac{\mathrm{d}w^*}{\mathrm{d}z} = w_x\frac{\mathrm{d}x^*}{\mathrm{d}z} + w_y\frac{\mathrm{d}y^*}{\mathrm{d}z} + w_z, \tag{3.10}$$

where all quantities are evaluated on the track. Thus, the derivative along the track generally differs from the partial derivative w_z.

If the computed background solution preserves reflection symmetry about $z = 0$, then

$$u(x, y, -z) = u(x, y, z), \tag{3.11}$$

$$v(x, y, -z) = v(x, y, z), \tag{3.12}$$

$$w(x, y, -z) = -w(x, y, z). \tag{3.13}$$

On the symmetry plane, these relations imply

$$w = 0, \qquad u_z = v_z = 0, \qquad w_x = w_y = 0. \tag{3.14}$$

The midplane root

$$\boldsymbol{x}_c = (x^*(0), y^*(0), 0) \tag{3.15}$$

is therefore a full 3D equilibrium. Defining

$$\gamma_{3D} = w_z(\boldsymbol{x}_c), \tag{3.16}$$

the full velocity Jacobian has the block form

$$J_{3D}(\boldsymbol{x}_c) = \begin{pmatrix} u_x & u_y & 0 \\ v_x & v_y & 0 \\ 0 & 0 & \gamma_{3D} \end{pmatrix}_{\boldsymbol{x}_c}. \tag{3.17}$$

Equation (3.10) then gives $\gamma_{\text{track}} = \gamma_{3D}$. When the in-plane eigenvalues form a complex pair, incompressibility supplies the consistency check

$$\operatorname{tr} J_{3D} = 2\alpha(0) + \gamma_{3D} = 0. \tag{3.18}$$

These relations test both the numerical derivatives and the assumed reflection symmetry; symmetry of the geometry alone does not prove that the computed solution preserves that symmetry.

For $\alpha(0) \neq 0$, the complex pair and $\gamma_{3D} = -2\alpha(0)$ have real parts of opposite sign. The midplane equilibrium is therefore a 3D saddle-focus, provided $|\beta| > 0$. Attraction in the symmetry plane is then accompanied by expansion in the depthwise direction, and conversely. Away from the symmetry plane, the eigenvalues of $J_\perp$ describe only the reduced fixed-depth field.

Background-fluid trajectories satisfy

$$\frac{\mathrm{d}\boldsymbol{X}}{\mathrm{d}t} = \overline{\boldsymbol{u}}(\boldsymbol{X}), \qquad \boldsymbol{X}(0) = \boldsymbol{X}_0. \tag{3.19}$$

Because the background field is steady, their paths are 3D streamlines. They represent passive background-fluid motion rather than finite-particle trajectories.

A nearly closed projection is treated initially as a recurrence candidate. A periodic orbit must satisfy

$$\boldsymbol{X}(T) = \boldsymbol{X}(0), \qquad T > 0, \tag{3.20}$$

within the stated numerical tolerance. Closure and orbital stability are assessed separately. In a streamwise-periodic calculation, a trajectory may instead satisfy

$$\boldsymbol{X}(T) = \boldsymbol{X}(0) + n\boldsymbol{\ell}, \qquad n \in \mathbb{Z}, \tag{3.21}$$

which represents a relative periodic trajectory advancing through n cells. A closed orbit confined to one cavity requires $n = 0$ and continued trapping to that cavity.

Cases of nearby trajectories are described initially as trajectory fans. A stream surface interpretation requires a continuous seed curve and a numerically resolved surface tangent to $\overline{\boldsymbol{u}}$. Identification as a stable or unstable invariant manifold additionally requires association with a specified equilibrium or periodic orbit and convergence to that object in forward or backward time, respectively [29]. The interpolation, trajectory-integration and recurrence calculations are assessed under refinement of the velocity representation, seed spacing and integration settings.

3.6 Preliminary particle method

The particle calculation connects a verified particle mesh to auxiliary Stokes solutions, hydrodynamic loads, leading particle motion and, subsequently, the inertial contribution. Development uses the existing reference solver structure, with targeted changes for the cavity geometry, numerical background and selected disturbance boundary model.

Each stage identifies the mathematical problem being solved, the meaning of its outputs and the checks required before those outputs enter the next stage.

3.6.1 Staged development and verification

Stage A: construct and check the particle mesh. The channel–cavity fluid domain is constructed with the spherical particle removed. The output is a particle-fitted mesh with identified physical boundaries and a record of the geometry, refinement parameters and mesh checks. Verification addresses particle clearance, boundary areas, complete boundary identification, fluid volume and element quality, together with periodic-face correspondence where that particle model is used. No background velocity field is needed to generate this mesh, although its geometry must match the intended background case.

Stage B: verify one prescribed translation. The first solver test prescribes unit particle translation in the streamwise direction, zero rotation and zero background flow:

$$\boldsymbol{U}_{\text{test}} = \boldsymbol{e}_x, \qquad \boldsymbol{\Omega}_{\text{test}} = \boldsymbol{0}, \qquad \overline{\boldsymbol{u}} = \boldsymbol{0}. \tag{3.22}$$

At the fixed test configuration, the auxiliary velocity $\boldsymbol{\phi}_x$ and physical pressure π_x solve

$$-\nabla\pi_x + \nabla^2\boldsymbol{\phi}_x = \boldsymbol{0}, \qquad \nabla\cdot\boldsymbol{\phi}_x = 0, \tag{3.23}$$

with $\boldsymbol{\phi}_x = \boldsymbol{e}_x$ on the sphere, $\boldsymbol{\phi}_x = \boldsymbol{0}$ on stationary walls, and the explicitly selected disturbance end conditions. No background-driven flow is included in this resistance test.

The outputs are one Stokes solution and all six associated force/torque components. Checks address imposed boundary values, incompressibility, solver convergence, load signs and sensitivity to numerical resolution. This is a prescribed-motion resistance test, not a force-free particle moving in the cached cavity flow. Acceptance tolerances and the numerical comparison used for this test will be stated with its results.

Stage C: determine the leading particle motion. After the single-mode calculation is checked, the same machinery is used for the three unit translations, three unit rotations and the background-driven problem. The matching numerical background is loaded for the background contribution. Their generalised loads determine the leading translation and rotation through a six-component matrix balance. An independent combined Stokes solve then checks the assembled motion and the position of the component fields.

Stage D: evaluate the cavity-specific inertial contribution. Only after the leading calculation has passed its checks is the selected cavity source evaluated using the leading fields and particle motion. The auxiliary fields are reused for signed reciprocal projections, and a matching forced Stokes calculation provides an independent numerical comparison where appropriate. The projected quantities enter the complete first-order load balances; they are not particle-velocity corrections by themselves. The disturbance-time closure, scaling and physical accuracy are assessed as described in Section 3.7.

3.6.2 Leading motion and matrix conventions

The leading particle calculation solves Eqs. (2.47)–(2.48) on a particle-fitted mesh. It uses the linear resistance–mobility formulation of Stokes flow [30]. All component problems use the same particle configuration, load convention, pressure treatment and applicable boundary and driving conditions.

Let $(\boldsymbol{\phi}_i, \pi_i)$, $i = 1, \ldots, 6$, denote the six rigid-motion Stokes solutions. The first three prescribe unit translations in x, y and z; the remaining three prescribe unit rotations about those axes. Each solution produces all three force components and all three torque components.

In the stationary-particle background-driven problem used for the mathematical notation here, the disturbance condition is

$$\boldsymbol{v}_b = -\overline{\boldsymbol{u}}(\boldsymbol{x}) \qquad \text{on the sphere.} \tag{3.24}$$

The generalised load columns from the six rigid-motion problems form the 6×6 signed resistance matrix R. The load of $\boldsymbol{v}_b$ is denoted by $\boldsymbol{g}_b$. With

$$\boldsymbol{c}_0 = \begin{pmatrix} \boldsymbol{U}_0 \\ \boldsymbol{\Omega}_0 \end{pmatrix}, \tag{3.25}$$

the leading disturbance force and torque balance is

$$R\boldsymbol{c}_0 + \boldsymbol{g}_b = \boldsymbol{0}. \tag{3.26}$$

This uses the proposed load ordering in Section 2.5.8. The motion components are ordered as $(U_{0x}, U_{0y}, U_{0z}, \Omega_{0x}, \Omega_{0y}, \Omega_{0z})$, with the corresponding force and torque ordering retained in every matrix and load vector.

The vector $\boldsymbol{g}_b$ is the load generated by the background-driven Stokes disturbance problem. It is distinct from the background-stress contribution to the complete finite-inertia particle balance. The matrix R uses the stated signed traction convention; its sign is not changed independently to produce a separately defined positive drag matrix.

The supplied reference implementation uses an equivalent background-mode convention. It applies the positive background trace on the sphere, computes the resulting load vector $\boldsymbol{b}$, and subtracts that mode when constructing the physical disturbance. It stores the six loads from each rigid-motion problem as a row of M. For the same boundary value problem, scaling and load convention, the correspondence is

$$R = M^T, \qquad \boldsymbol{g}_b = -\boldsymbol{b}, \qquad \boldsymbol{c}_0 = \texttt{res}. \tag{3.27}$$

Consequently,

$$R\boldsymbol{c}_0 + \boldsymbol{g}_b = \boldsymbol{0} \quad \Longleftrightarrow \quad M^T\boldsymbol{c}_0 = \boldsymbol{b}. \tag{3.28}$$

This is the convention implemented by `res = np.linalg.solve(M.T, b)`. The transpose and background sign are therefore retained together.

Writing $\boldsymbol{v}_{+b}$ for the positive-background boundary mode, the physical leading disturbance can be expressed as

$$\boldsymbol{v}_0 = \sum_{i=1}^{6} c_{0i}\boldsymbol{\phi}_i + \boldsymbol{v}_b = \sum_{i=1}^{6} c_{0i}\boldsymbol{\phi}_i - \boldsymbol{v}_{+b}. \tag{3.29}$$

The independent combined solve imposes

$$\boldsymbol{v}_0 = \boldsymbol{U}_0 + \boldsymbol{\Omega}_0 \times \boldsymbol{r} - \overline{\boldsymbol{u}}(\boldsymbol{x}) \qquad \text{on the sphere.} \tag{3.30}$$

All three components of the numerical cavity background are subtracted. Replacing the analytic background definition alone is insufficient if a later boundary expression still subtracts only the original straight-duct streamwise component.

The leading-stage sequence contains seven component problems and one independent combined check:

6 rigid-motion solves + 1 background solve + 1 combined check = 8 Stokes solves.

The initial unit-x translation is one of the six rigid-motion problems, not a ninth distinct component problem. Its solution can be reused when the configuration and all numerical settings agree.

Reciprocal-theorem volume-integral diagnostics provide further consistency checks [31]. These comparisons require an explicitly stated integral identity and consistent auxiliary fields, forcing, load conventions and boundary terms. Together, these tests assess the numerical Stokes response; they do not by themselves establish physical inertial lift or validate the finite-inertia approximation.

3.6.3 Existing reference calculation and proposed verification case

The completed preliminary calculation at $\boldsymbol{x}_p = (0, -0.5, 0)$, $\kappa = 0.05$ and $\mathrm{Re} = 10$ is reported in Section 4.8. It provides an initial symmetry-position test of the resistance and mobility calculation. Its numerical results remain associated with that cavity configuration.

The proposed next single-position verification places the sphere in the main channel above the cavity:

$$\begin{gathered} \boldsymbol{x}_{p,\mathrm{test}} = (0, 0.25, z_{\mathrm{test}}), \qquad z_{\mathrm{test}} \neq 0, \\ \kappa = \frac{\widehat{a}}{\widehat{H}_c} = 0.05, \qquad \mathrm{Re} = 10, \qquad \mathrm{Re}_p = \kappa^2 \mathrm{Re} = 0.025. \end{gathered} \tag{3.31}$$

The proposed verification sphere is positioned above the cavity mouth, halfway through the upper-channel height, and away from the depthwise symmetry plane. The selected depthwise offset will be recorded with the calculation inputs. Figure 2.1 shows its projection onto the x–y plane.

For this geometry and particle radius, the surface gaps to the upper wall and the nearer depthwise wall are

$$d_{\mathrm{top}} = 0.5 - 0.25 - \kappa = 0.20, \qquad d_{\mathrm{side}} = \frac{W}{2} - |z_{\mathrm{test}}| - \kappa = 1.0125 - |z_{\mathrm{test}}|. \tag{3.32}$$

The depthwise offset must satisfy $0 < |z_{\mathrm{test}}| < 1.0125$ to avoid intersection with a side wall. The minimum wall clearance at this proposed position is

$$d_{\min} = \min\{0.20,\ 1.0125 - |z_{\mathrm{test}}|\}\,. \tag{3.33}$$

For the pilot value $z_{\mathrm{test}} = 0.1$, the upper-wall gap remains smaller, giving $d_{\min} = 0.20$ and $d_{\min}/\kappa = 4$. This pilot value is not treated as a finalised input. The clearance will be recalculated for the adopted offset and checked against the particle-fitted mesh.

The nonzero depthwise offset avoids relying only on components suppressed by reflection symmetry. It does not guarantee a particular lift magnitude or sign.

To assess the leading response, the calculation will compare

$$\begin{gathered} \boldsymbol{U}_0 \quad \text{with} \quad \overline{\boldsymbol{u}}(\boldsymbol{x}_{p,\mathrm{test}}), \\ \boldsymbol{\Omega}_0 \quad \text{with} \quad \frac{1}{2}\nabla \times \overline{\boldsymbol{u}}(\boldsymbol{x}_{p,\mathrm{test}}). \end{gathered} \tag{3.34}$$

These reference quantities are motivated by the force-free and torque-free small-sphere limits of the classical Faxén relations in unbounded creeping flow [30]. They are dia-

gnostics rather than imposed equalities: finite particle size, background-flow curvature and confinement can alter the resolved translation and rotation. No separate Faxén correction is added to the resolved-sphere solution.

3.6.4 Staged adaptation of the particle calculation

The particle calculation will be adapted and verified in stages using the existing reference solver structure. Previously verified components will be retained where their geometry, boundary conditions and normalisation remain applicable. Development will proceed through the particle-mesh checks, one prescribed-translation test, the complete leading-motion calculation and, subsequently, the cavity-specific inertial contribution.

The currently supplied staged plan provides mesh generation and geometric checks (Stage A), followed by a single prescribed unit-translation Stokes test with zero background flow (Stage B). The translation test imposes zero disturbance on the finite end planes. Periodic particle constraints, numerical background transfer, the complete leading-motion calculation and the cavity-specific inertial correction remain to be integrated into this driver.

For the proposed main channel free particle calculation in Eq. (3.31), the sphere will be free to translate and rotate. The proposal formulation is periodic with respect to the particle and holds the imposed pressure gradient at its particle-free background value. This specifies the periodic fixed-gradient problem in Section 2.5.4. It is an explicit project modelling choice, not a consequence of loading a periodic background.

The finite-end translation test is an initial implementation check. Before the proposed periodic fixed-gradient particle calculation is performed, periodic velocity and pressure-remainder constraints will be implemented and verified. The prescribed translation test will then be repeated for that boundary value problem. Stage C will use the same verified periodic operator, load convention and driving constraint.

A sphere-fitted mesh for the proposed configuration will use local refinement around the particle and a gradual transition to the bulk mesh. Initial trial targets are $h_p = 0.01$ and $h_b = 0.08$ in cavity-depth units; these are not converged values. Geometry and transfer checks will follow Section 3.1. Background transfer is introduced for Stage C, not for the zero-background translation test.

Before the leading response is accepted, the reconstructed total velocity must satisfy the rigid particle boundary condition, the applicable wall and periodic conditions, and the discrete incompressibility constraint. Matrix assembly, combined-field agreement and load extraction must also pass their stated checks.

3.7 Planned stationary-device-frame inertial correction; under assessment

Chapter 4

Results to Date

4.1 Background-flow verification

The background calculations use the common targets $U_b = 1$ and $Q = A_{\mathrm{ch}} = 1.0625$. The available verification record for the periodic $\mathrm{Re} = 10$ medium-source field is summarised in Table 4.1. The topology figures presented below are labelled with the nominal base-source resolution $48 \times 24 \times 32$; the medium-source checks do not, by themselves, certify those other fields.

Table 4.1: Available verification metrics for the periodic $\mathrm{Re} = 10$ medium background source ($66 \times 33 \times 44$).

Metric	Value
Target bulk velocity	1
Achieved bulk velocity	0.999950323641112
Target flux	1.0625
Achieved flux	1.062447218869
Relative flux error	4.97×10^{-5}
Bulk-velocity tolerance	10^{-4}
Periodic velocity mismatch	2.80×10^{-14}
Volume/classification discrepancy	6.24×10^{-12}

The achieved bulk velocity satisfies the stated 10^{-4} tolerance. The reported periodic mismatch supports face matching, and the volume/classification discrepancy is below the recorded 10^{-10} tolerance. These checks establish consistency of the reported field with selected numerical constraints, rather than mesh independence.

4.2 Fixed-depth background-flow structure

Figures 4.1–4.3 show the periodic, Poiseuille and quadratic cases over the displayed Reynolds numbers and retained depths. The curves are integral curves of the fixed-depth in-plane field (u, v), while the colour represents w. They are not projections of full 3D trajectories. The yellow $w = 0$ contours do not by themselves identify invariant boundaries, and plotted roots on solid boundaries are excluded from interior critical-point classification.

All three cases show a dominant cavity recirculation whose position and shape vary with Reynolds number and depth. Between $\mathrm{Re} = 10$ and 100, the selected midplane root moves towards the cavity mouth and from the upstream to the downstream side. The outer retained slices show substantially different patterns from the midplane. The largest plotted depth, $z = 0.9296875$, is an interior sample; the physical side wall is at $z = 1.0625$.

The periodic and Poiseuille patterns are visually close. The quadratic case shows changes in the inlet region and in the cavity diagnostics. Its colour scale spans approximately ± 0.251, compared with ± 0.136 in the other two mosaics, so equal colours across the figures do not represent equal depthwise velocities.

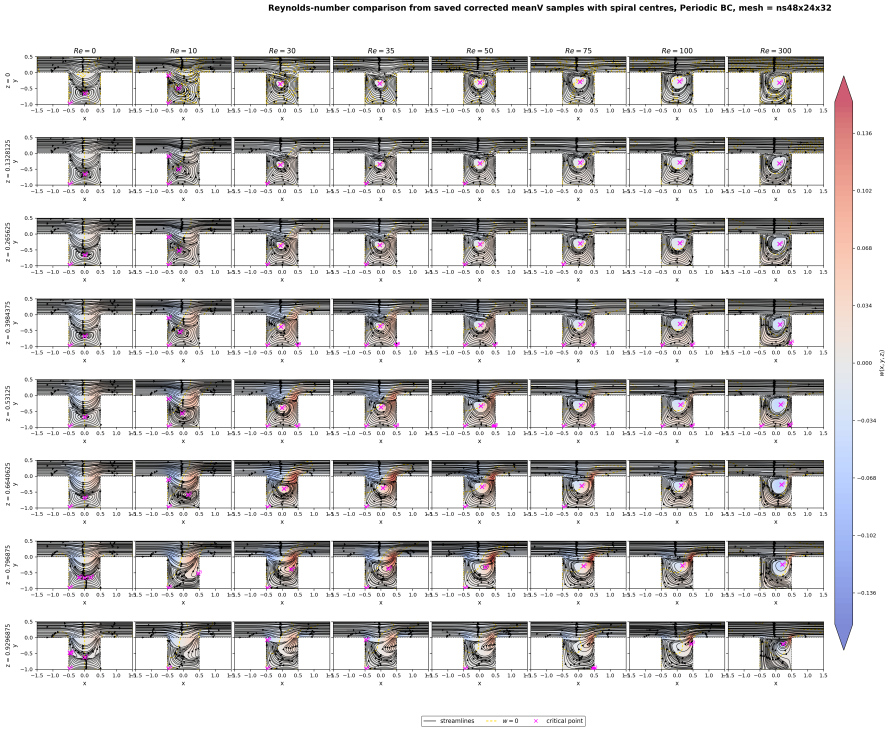


Figure 4.1: Periodic background field on the nominal $48 \times 24 \times 32$ source mesh. Columns show $\mathrm{Re} = 0, 10, 30, 35, 50, 75, 100, 300$ and rows show the retained non-negative depths. Black curves depict the fixed-depth (u, v) field; colour indicates w, yellow dashed curves indicate $w = 0$, and magenta marks are plotted root candidates. Boundary marks are not accepted as interior equilibria. The panel-specific colour bar must be used when comparing amplitudes.

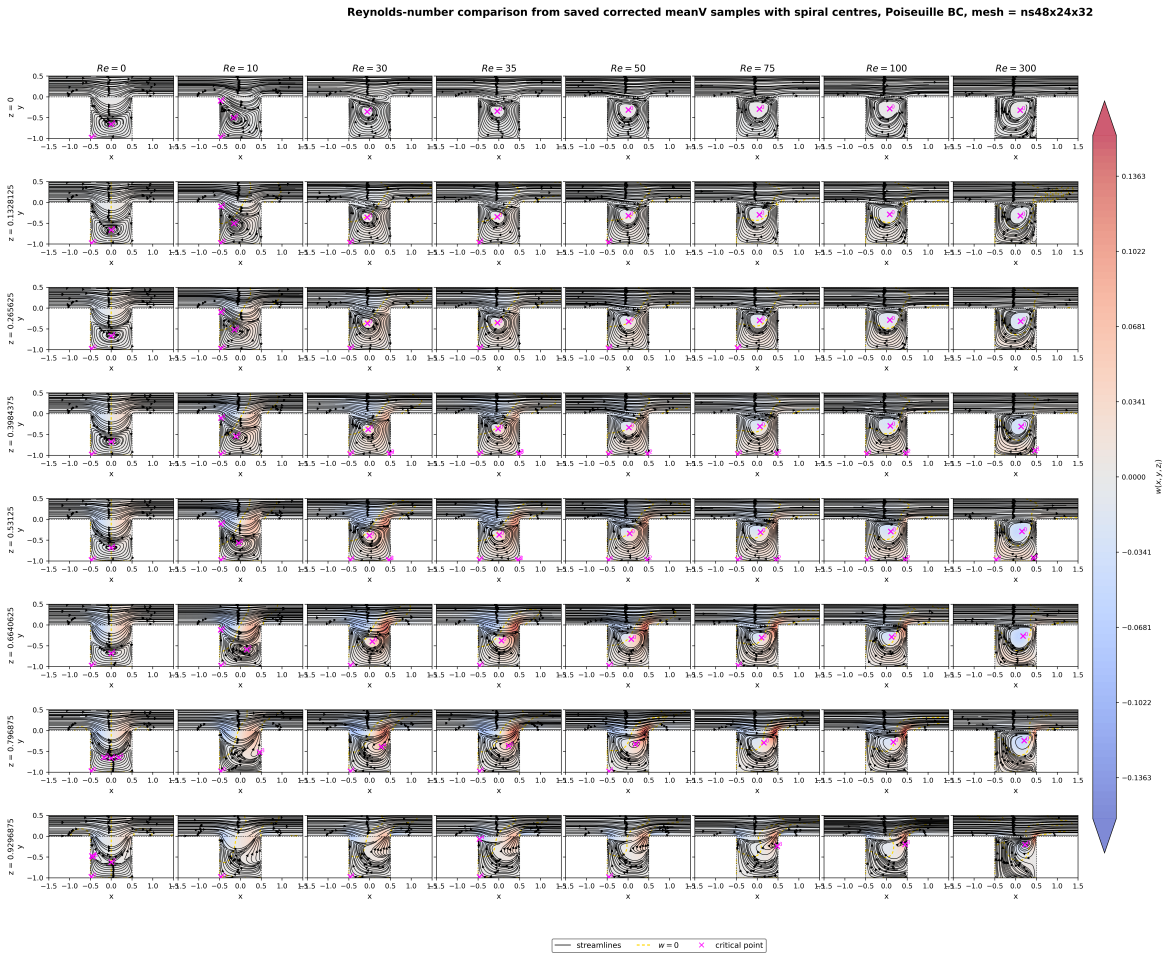


Figure 4.2: Poiseuille inlet–outlet background field on the nominal $48 \times 24 \times 32$ source mesh. Columns show $\mathrm{Re} = 0, 10, 30, 35, 50, 75, 100, 300$ and rows show the retained non negative depths. Black curves depict the fixed-depth (u, v) field; colour indicates w, yellow dashed curves indicate $w = 0$, and magenta marks are plotted root candidates. Boundary marks are not accepted as interior equilibria. The panel-specific colour bar must be used when comparing amplitudes.

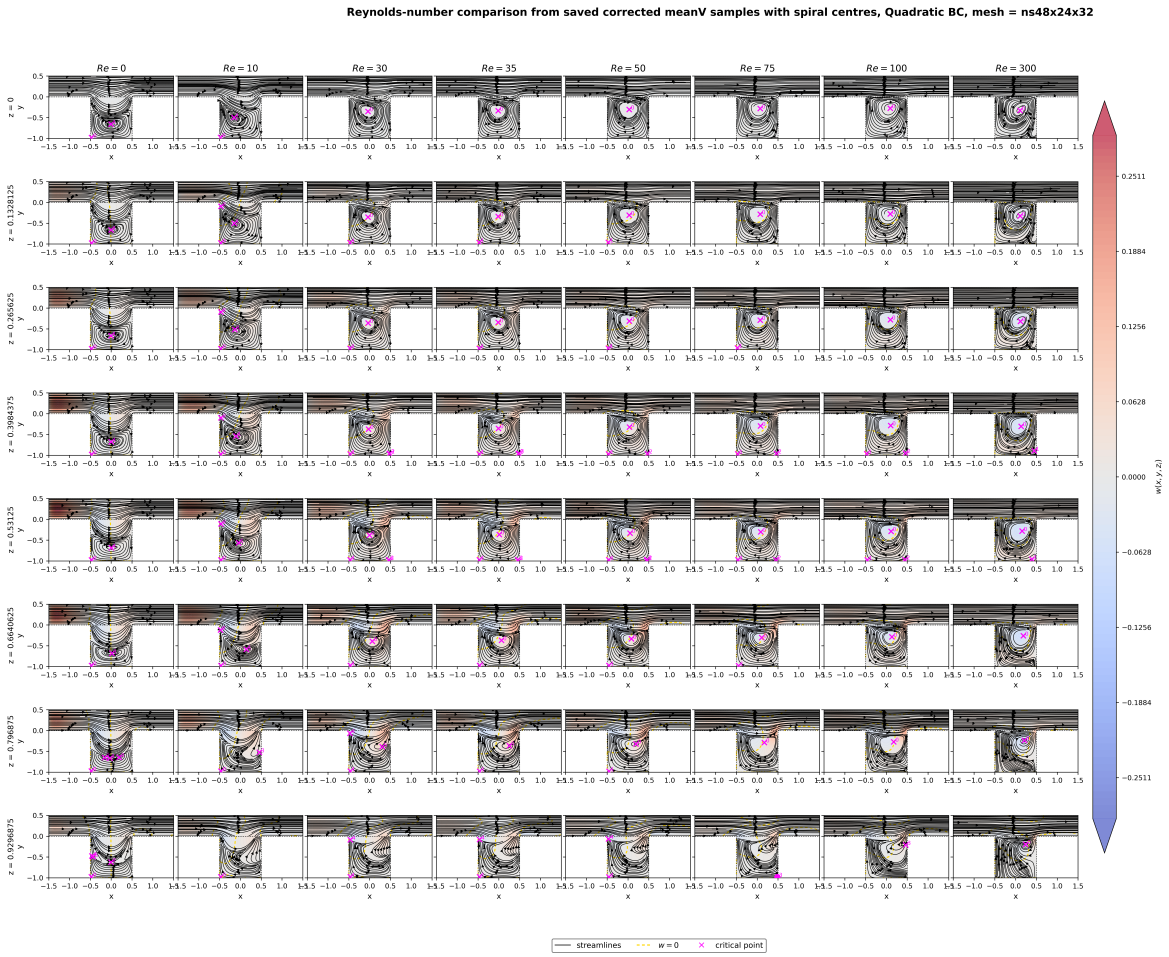


Figure 4.3: Quadratic inlet–outlet background field on the nominal $48 \times 24 \times 32$ source mesh. Columns show $\mathrm{Re} = 0, 10, 30, 35, 50, 75, 100, 300$ and rows show the retained non negative depths. Black curves depict the fixed-depth (u, v) field; colour indicates w, yellow dashed curves indicate $w = 0$, and magenta marks are plotted root candidates. Boundary marks are not accepted as interior equilibria. The panel-specific colour bar must be used when comparing amplitudes.

4.3 Principal centre-track

Figures 4.4–4.6 compare the sampled centre track coordinates for the periodic, Poiseuille and quadratic background fields, with the lower and higher Reynolds number groups displayed separately. The periodic and Poiseuille tracks are visually similar over the displayed ranges, whereas the quadratic case shows differences in the selected root positions. The Re = 10 periodic–Poiseuille comparison is quantified in Section 4.6, and the Re = 100 comparison in Section 4.7. Comparisons at the remaining Reynolds numbers are qualitative.

At Re = $75, 100, 300$, the sampled streamwise coordinate increases with positive depth. The vertical coordinate does not vary monotonically with Reynolds number: in all three formulations, the midplane root at Re = 300 lies deeper than that at Re = 100. Each coordinate uses its own vertical axis, and the axis ranges differ between panels; comparisons therefore use coordinate values rather than the apparent positions or crossings of the plotted curves.

Several tracks bend sharply between their outermost samples, and the displayed depth ranges differ. These features require checks of branch continuation and sampling sensitivity. The last plotted point does not by itself identify a physical termination of the root branch.

For Re = 10, the periodic and Poiseuille panels show the six spiral samples through $z = 0.6640625$. An additional continued root at $z = 0.796875$ is classified as a repelling node and is shown separately in Fig. 4.13. Thus, these panels display the spiral portion of the selected branch, while the comparison figure includes the outer node.

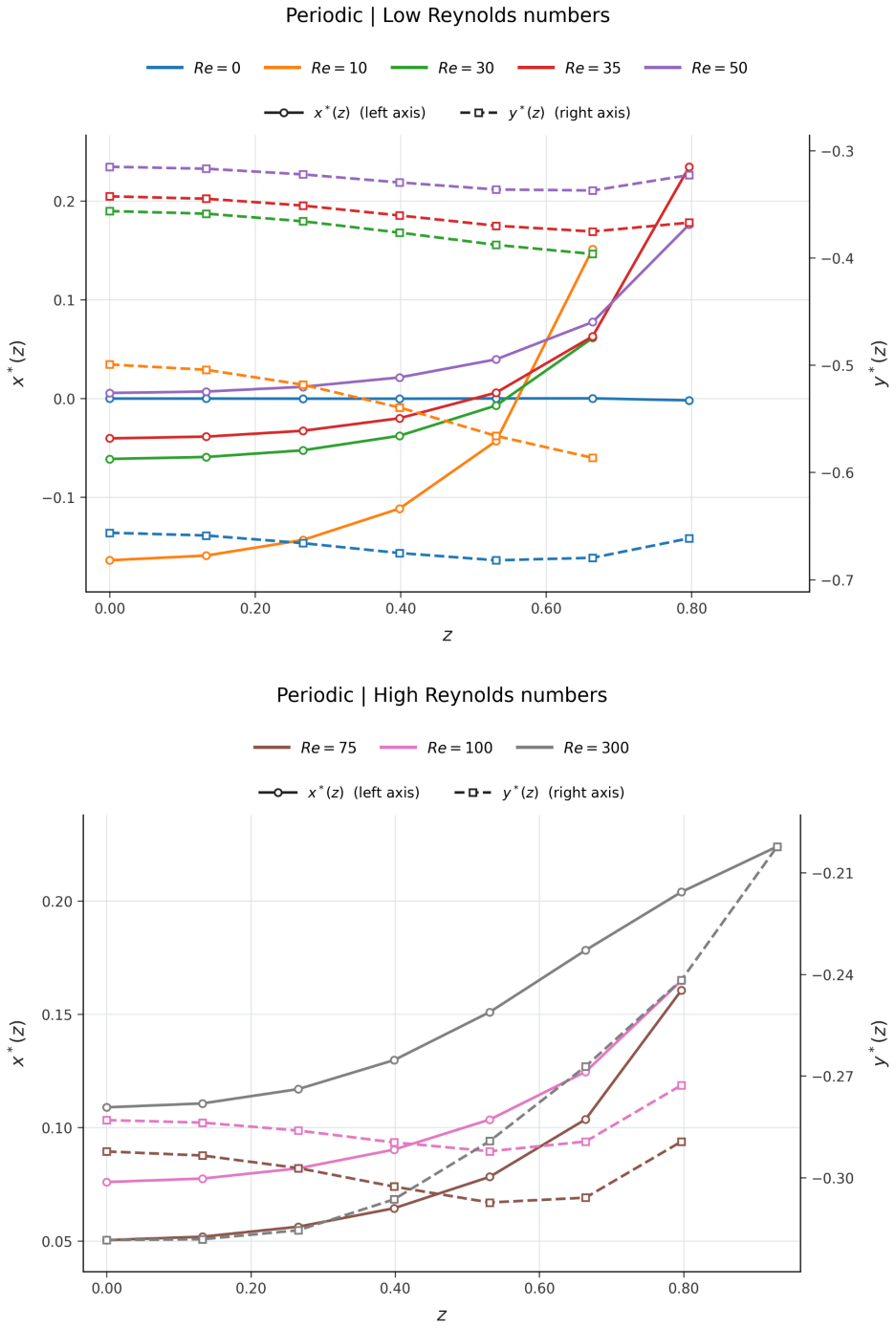


Figure 4.4: Principal centre-track coordinates for the periodic background fields on the nominal $48 \times 24 \times 32$ source mesh. Upper panel: $\mathrm{Re} = 0, 10, 30, 35, 50$; lower panel: $\mathrm{Re} = 75, 100, 300$. Solid lines with circular markers show $x^*(z)$ on the left axis; dashed lines with square markers show $y^*(z)$ on the right axis. Colours identify Reynolds numbers as specified in the legends. Markers denote the sampled roots; connecting lines are guides to the eye. The $\mathrm{Re} = 10$ curve shows only the spiral portion of the branch.

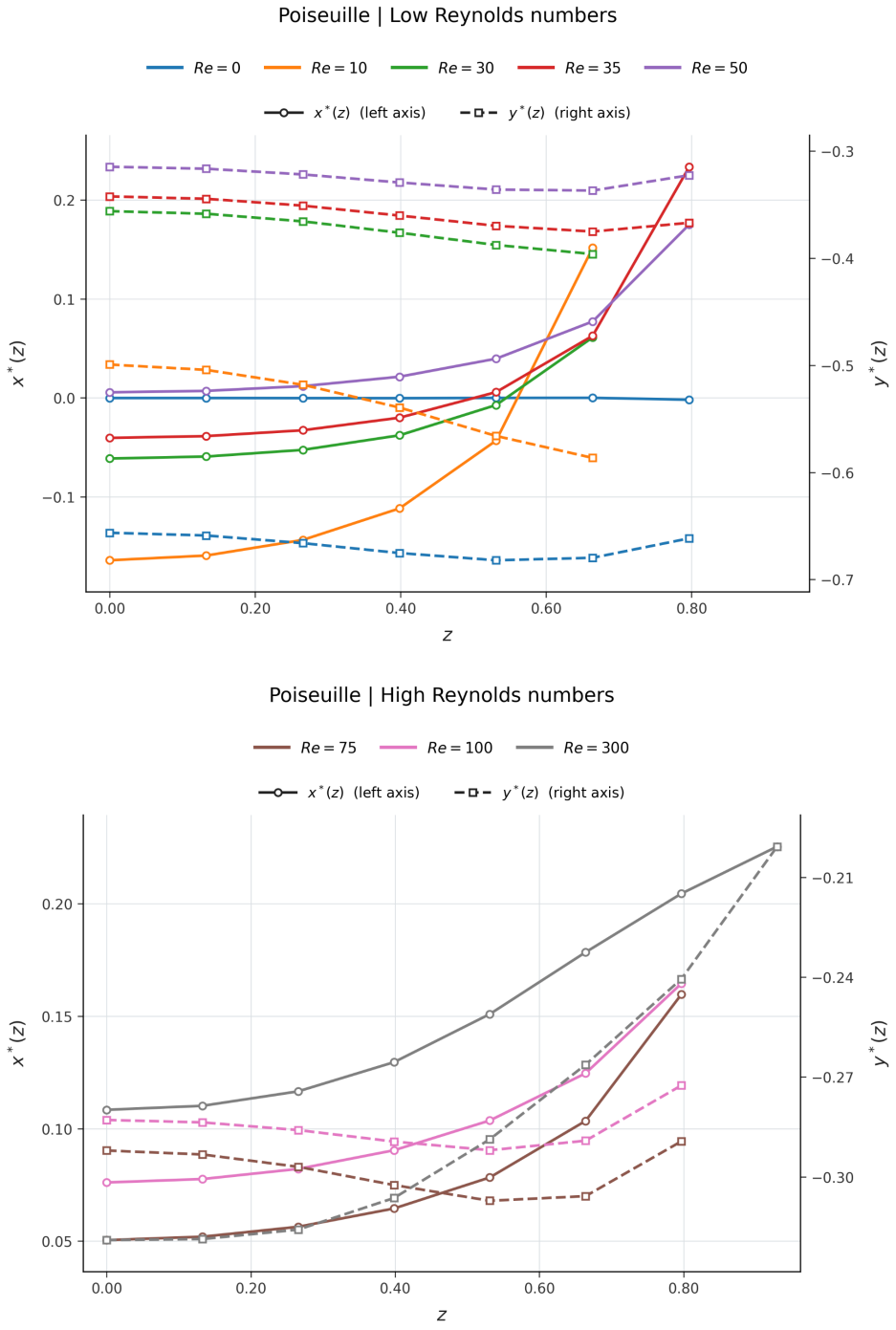


Figure 4.5: Principal centre-track coordinates for the Poiseuille inlet–outlet background fields on the nominal $48 \times 24 \times 32$ source mesh. Upper panel: $\mathrm{Re} = 0, 10, 30, 35, 50$; lower panel: $\mathrm{Re} = 75, 100, 300$. Solid lines with circular markers show $x^*(z)$ on the left axis; dashed lines with square markers show $y^*(z)$ on the right axis. Colours identify Reynolds numbers as specified in the legends. Markers denote the sampled roots; connecting lines are guides to the eye. The $\mathrm{Re} = 10$ curve shows only the spiral portion of the branch.

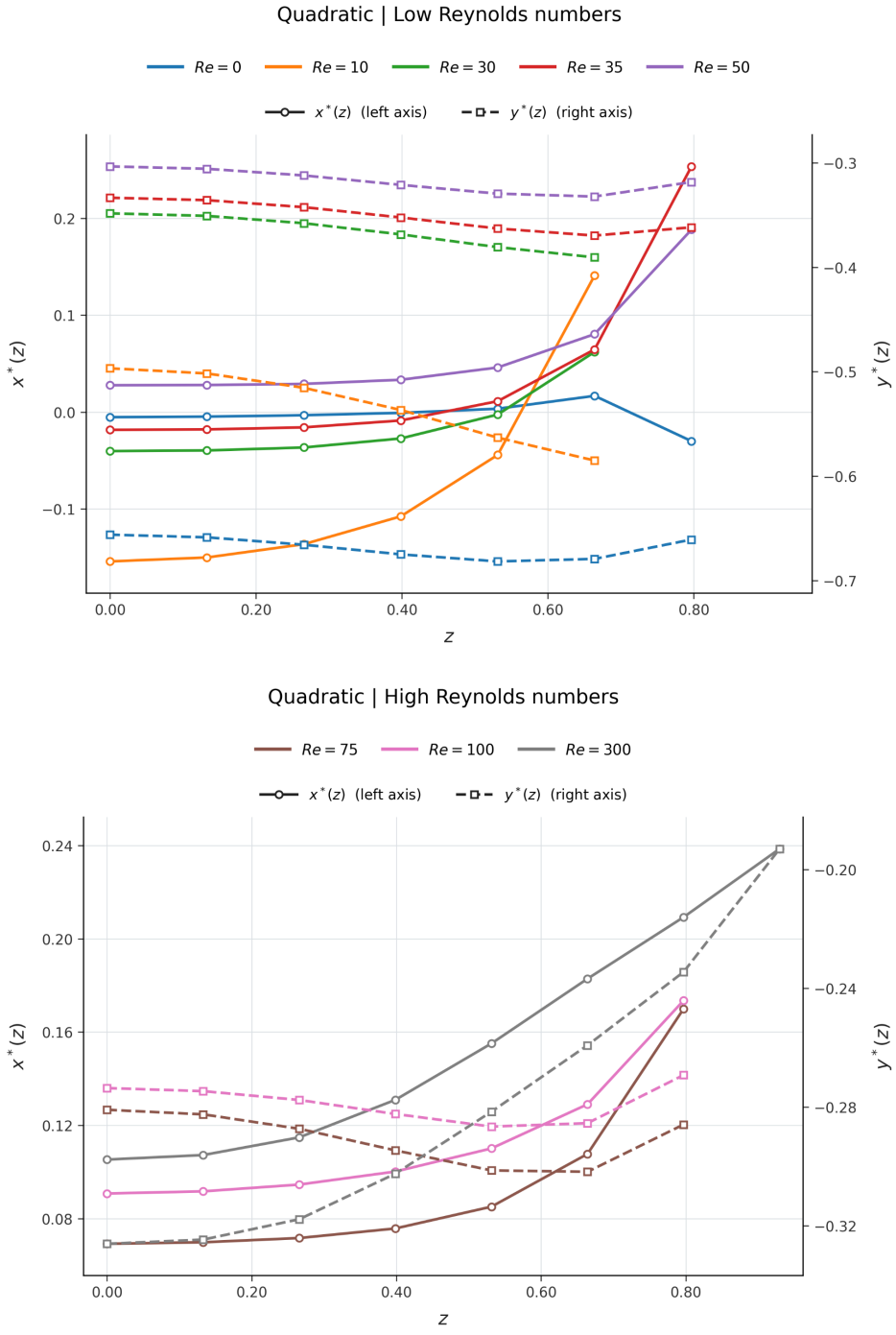


Figure 4.6: Principal centre-track coordinates for the quadratic inlet–outlet background fields on the nominal $48 \times 24 \times 32$ source mesh. Upper panel: $\mathrm{Re} = 0, 10, 30, 35, 50$; lower panel: $\mathrm{Re} = 75, 100, 300$. Solid lines with circular markers show $x^*(z)$ on the left axis; dashed lines with square markers show $y^*(z)$ on the right axis. Colours identify Reynolds numbers as specified in the legends. Markers denote the sampled roots; connecting lines are guides to the eye.

4.4 Depthwise velocity on the centre-track

Figures 4.7–4.9 compare $w^*(z)$ on the selected branches. For $z > 0$, positive values indicate motion locally away from the symmetry plane and negative values indicate motion locally towards it. These are pointwise velocities on the track, not an integrated exchange flux.

For periodic and Poiseuille driving, the $\mathrm{Re} = 10, 30, 35$ curves have the outward sign at the first positive-depth sample, whereas the $\mathrm{Re} = 50$ curve has the inward sign there. The latter becomes positive farther from the midplane. The $\mathrm{Re} = 75$ curve also changes sign over the retained depths; the $\mathrm{Re} = 100$ and 300 curves remain negative at their displayed positive-depth samples.

The quadratic case changes near-midplane sign earlier: the $\mathrm{Re} = 10$ curve is positive, while the $\mathrm{Re} = 30$ curve has a small negative value at the first positive-depth sample. This small signal needs confirmation from the underlying derivatives and numerical uncertainty. The larger negative values at higher Reynolds numbers show that the reversal is not confined to a single plotted point. The $\mathrm{Re} = 0$ curves remain close to zero on this plotting scale.

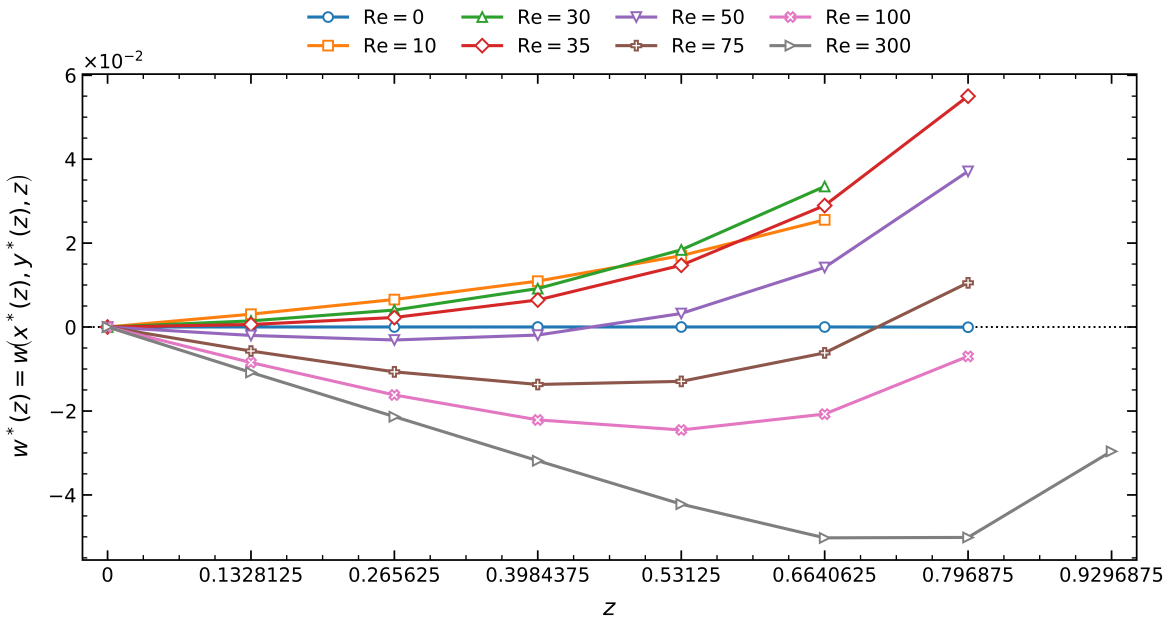


Figure 4.7: Depthwise velocity $w^*(z)$ on the periodic principal centre-track. Markers indicate retained samples. A sign change between samples suggests a zero on a continuous branch, but does not locate it accurately or verify a 3D equilibrium. Curves are shown only over their plotted branch intervals.

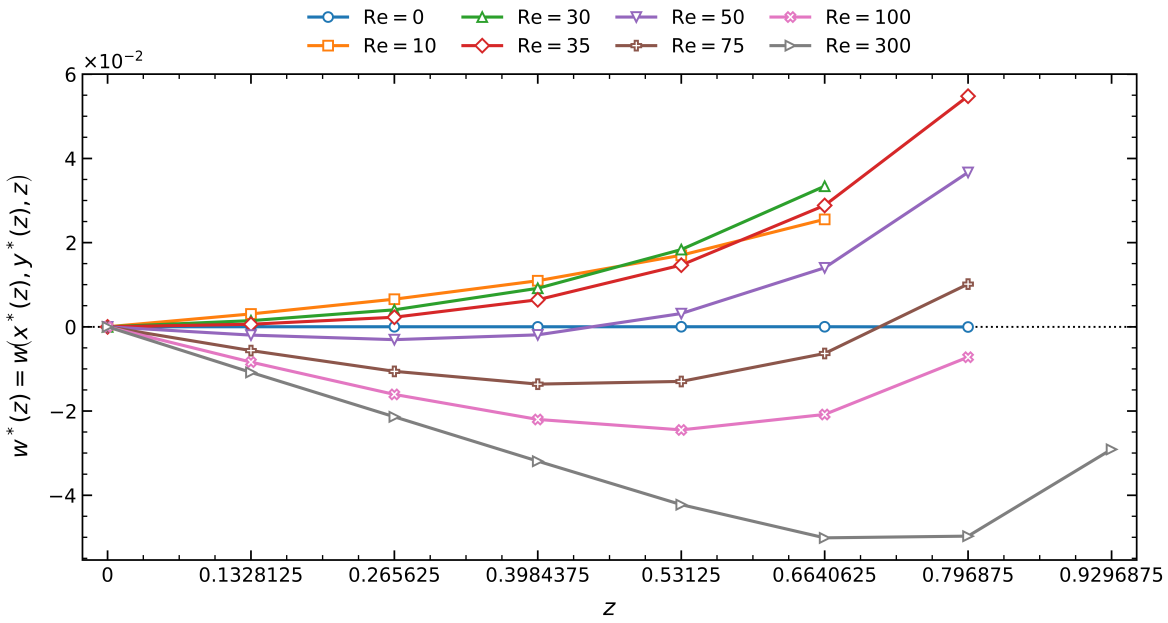


Figure 4.8: Depthwise velocity $w^*(z)$ on the Poiseuille principal centre-track. Markers indicate retained samples. A sign change between samples suggests a zero on a continuous branch, but does not locate it accurately or verify a 3D equilibrium. Curves are shown only over their plotted branch intervals.

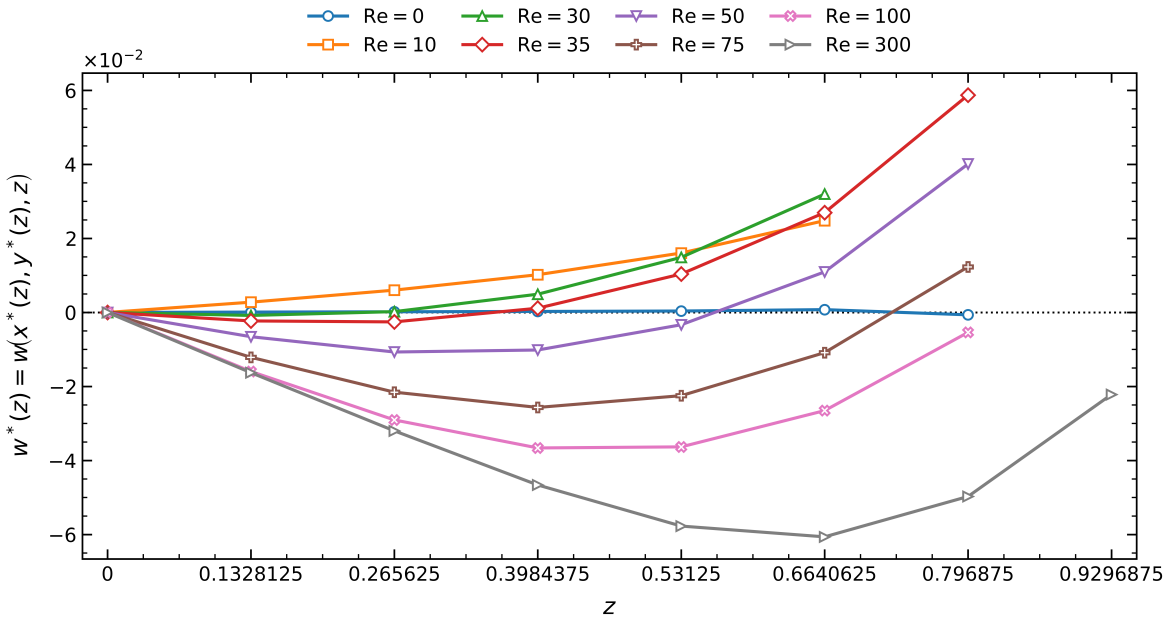


Figure 4.9: Depthwise velocity $w^*(z)$ on the quadratic principal centre-track. Markers indicate retained samples. A sign change between samples suggests a zero on a continuous branch, but does not locate it accurately or verify a 3D equilibrium. Curves are shown only over their plotted branch intervals.

4.5 In-plane eigenvalues and provisional transition intervals

Figures 4.10–4.12 show $\alpha(z)$ and the signed rotation diagnostic $\beta_{\text{rotation}}(z)$. Solid curves use the left axis and dashed curves the right axis. For a complex pair, the signed diagnostic is

$$\beta_{\text{rotation}} = \operatorname{sgn}(v_x - u_y)\,|\operatorname{Im}\lambda_1|\,. \tag{4.1}$$

Its sign follows in-plane vorticity; it is not a third eigenvalue. Where the pair is complex, negative and positive α identify attracting and repelling fixed-depth spirals, respectively.

The displayed periodic and Poiseuille values of $\alpha(0)$ are negative at $\mathrm{Re} = 35$ and positive at $\mathrm{Re} = 50$. In the quadratic case they are negative at $\mathrm{Re} = 10$ and slightly positive at $\mathrm{Re} = 30$. Together with the w^* plots, these observations suggest the candidate intervals

$$\begin{aligned} 35 &< \mathrm{Re}_c^{\text{periodic}} < 50, \\ 35 &< \mathrm{Re}_c^{\text{Poiseuille}} < 50, \\ 10 &< \mathrm{Re}_c^{\text{quadratic}} < 30. \end{aligned} \tag{4.2}$$

Here Re_c denotes a candidate local sign change on the selected midplane branch. These intervals require confirmation that the branch is continuous and that the endpoint signs exceed their numerical uncertainty. The images suggest a range for this local transition, but do not determine a precise value of Re_c.

The nonzero values of the signed rotation diagnostic β_{rotation} remain negative in the plotted cases. The reported sign change in α therefore concerns local in-plane attraction or repulsion, rather than a demonstrated change in rotational sense. At some depths farther from the midplane, $\alpha(z)$ has the opposite sign from $\alpha(0)$. Consequently, the local classification must be stated separately for each depth. Where the rotation diagnostic is close to zero or changes sharply between neighbouring samples, the calculated eigenvalues must be checked before the critical point is classified as a spiral.

The small nonzero values of α reported at $\mathrm{Re} = 0$ must also be assessed against uncertainty in the velocity derivatives and critical-point locations. Without that assessment, they are not treated as evidence of an established local transition.

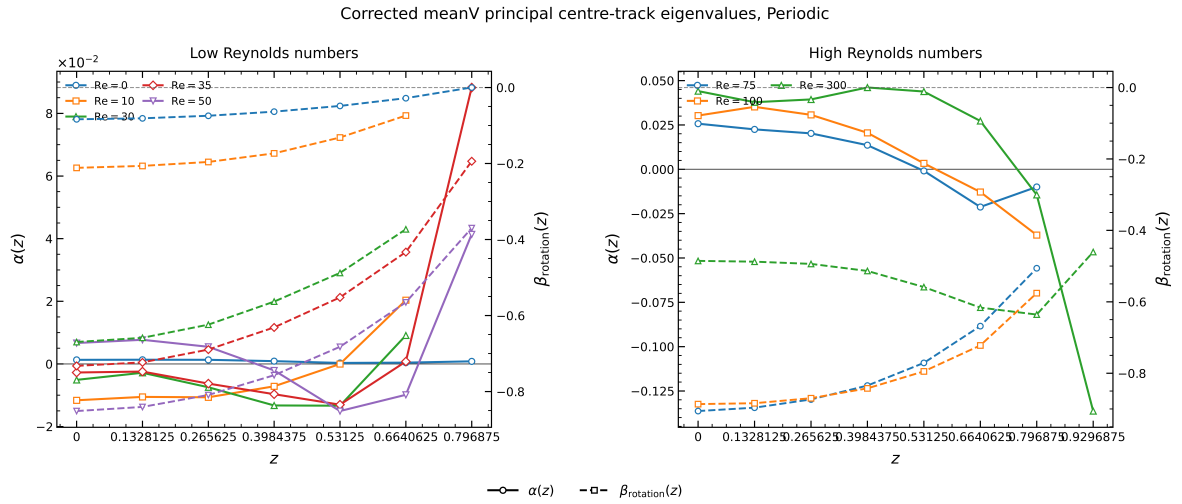


Figure 4.10: In-plane eigenvalue diagnostics on the periodic centre-track. Solid curves show α on the left axis and dashed curves show β_{rotation} on the right axis; Reynolds number colours are identified in the panels. The two axes have different scales, and the left-axis scale differs between panels. These are fixed-depth diagnostics away from the symmetry plane.

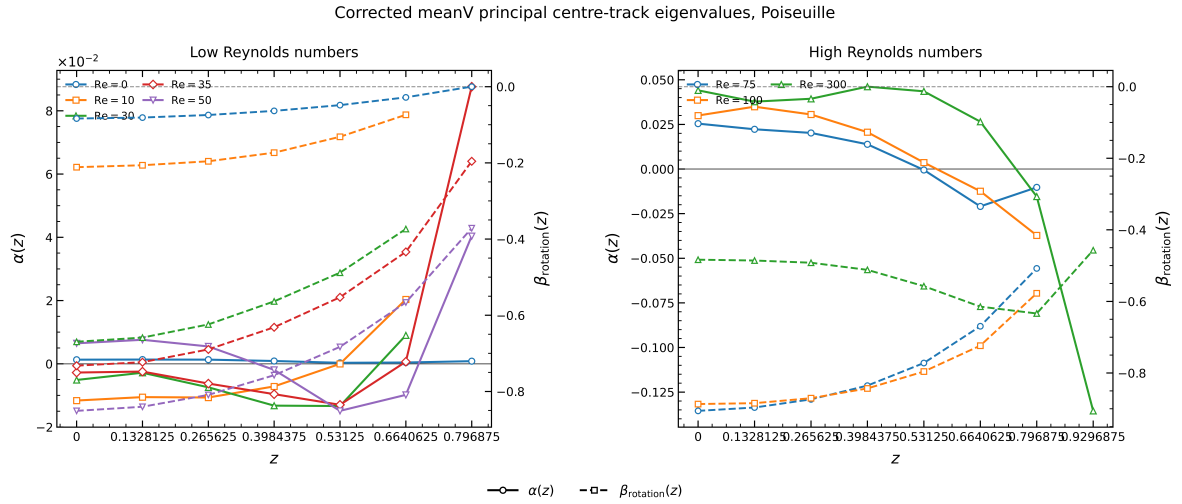


Figure 4.11: In-plane eigenvalue diagnostics on the Poiseuille centre-track. Solid curves show α on the left axis and dashed curves show β_{rotation} on the right axis; Reynolds number colours are identified in the panels. The two axes have different scales, and the left-axis scale differs between panels. These are fixed-depth diagnostics away from the symmetry plane.

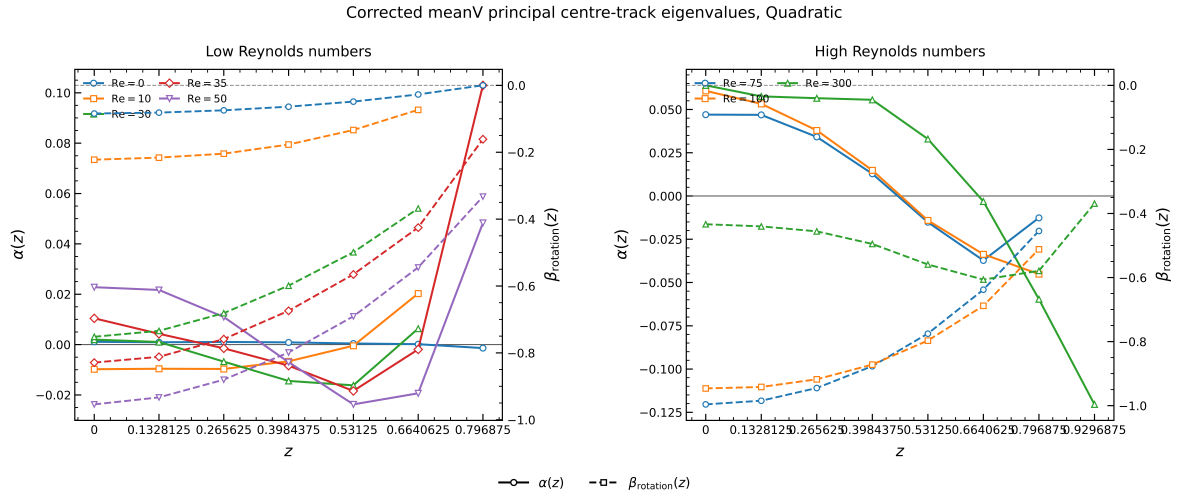


Figure 4.12: In-plane eigenvalue diagnostics on the quadratic centre-track. Solid curves show α on the left axis and dashed curves show β_{rotation} on the right axis; Reynolds number colours are identified in the panels. The two axes have different scales, and the left-axis scale differs between panels. These are fixed-depth diagnostics away from the symmetry plane.

4.6 Low-Reynolds number boundary-formulation comparison

Figure 4.13 compares the low-Reynolds number schematic of Torczynski and O'Hern [10] with the periodic and Poiseuille in-plane-root loci at $\mathrm{Re} = 10$. The numerical panel shows their (z, x) projections. Quantitative comparison of the sampled fields confirms close agreement at the nominal $48 \times 24 \times 32$ source resolution.

The comparison addresses whether the cavity recirculation is sensitive to replacing a finite inlet–outlet domain by a streamwise-periodic cell at the same target throughput. Here, "Poiseuille" denotes the inlet–outlet calculation with a fully developed rectangular-duct inlet profile; it does not imply that the velocity remains fully developed through the cavity. In the periodic calculation, the velocity and pressure remainder match across the streamwise faces, and the imposed pressure gradient is adjusted to achieve the target mean velocity. The inlet–outlet solution also depends on the inlet profile, the upstream and downstream lengths, and the outlet condition. Both formulations use $U_b = 1$, $Q = U_b A_{\text{ch}} = 17/16$ and the same mean-velocity definition of Re. Matching these quantities permits a controlled comparison, but does not impose identical pressure distributions.

Torczynski and O'Hern [10, p. 2, Simulations] used a cavity depth and length of one, channel height 0.5, and depthwise half-width 1.0625. Their inlet and outlet lie one cavity depth upstream and downstream of the cavity. These dimensions agree with the present geometry after shifting their streamwise origin to the cavity-mouth

centre. Their Reynolds number is also based on the cross-sectional mean velocity and cavity depth. Their model therefore provides an appropriate inlet–outlet reference, rather than a periodic benchmark. In particular, they prescribed a fully developed inlet profile and a natural outflow condition. Exact reproduction would additionally require the same outlet formulation and an assessment of discretisation differences.

The main-channel flow drives circulation within the cavity through the velocity gradients and stresses across its mouth. In three dimensions, this circulation is coupled to depthwise transport. Torczynski and O'Hern [10, p. 2, Results; Fig. 10] describe low-Reynolds-number streamlines entering near the channel midplane, spiralling towards the central cavity region and leaving towards the sidewalls. Their schematic distinguishes a point that attracts streamlines within the midplane from an emanating streamline that carries fluid away in the depthwise direction. Attraction in a planar plot therefore does not imply attraction in the full three-dimensional flow.

This interpretation follows locally from reflection symmetry and incompressibility. At a midplane equilibrium, the velocity gradient matrix separates into an in-plane block and a depthwise eigenvalue $\gamma_{3D} = \partial\overline{w}/\partial z$. If the in-plane eigenvalues are $\alpha \pm \mathrm{i}\omega$, with $\omega \neq 0$, then

$$2\alpha + \gamma_{3D} = 0. \tag{4.3}$$

Thus, an attracting in-plane spiral, $\alpha < 0$, is accompanied by depthwise expansion, $\gamma_{3D} > 0$. The equilibrium is a three-dimensional saddle-focus. This supplies a local explanation for the low-Re pattern in the paper; a global connection to the channel still requires integration of three-dimensional streamlines.

Figure 4.13(b) compares the periodic and Poiseuille loci of fixed-depth roots, defined by $\overline{u}(x^*, y^*, z) = \overline{v}(x^*, y^*, z) = 0$. Away from $z = 0$, $\overline{w}(x^*, y^*, z)$ need not vanish, so these roots are generally not 3D stagnation points. Joining their coordinates also does not produce a streamline: the root locus need not be tangent to the local velocity. Its near-overlap between formulations shows agreement in the location of the in-plane circulation centres, but cannot by itself verify the emanating streamline drawn in the literature schematic. The arrows and outer continuations on the root locus are schematic annotations.

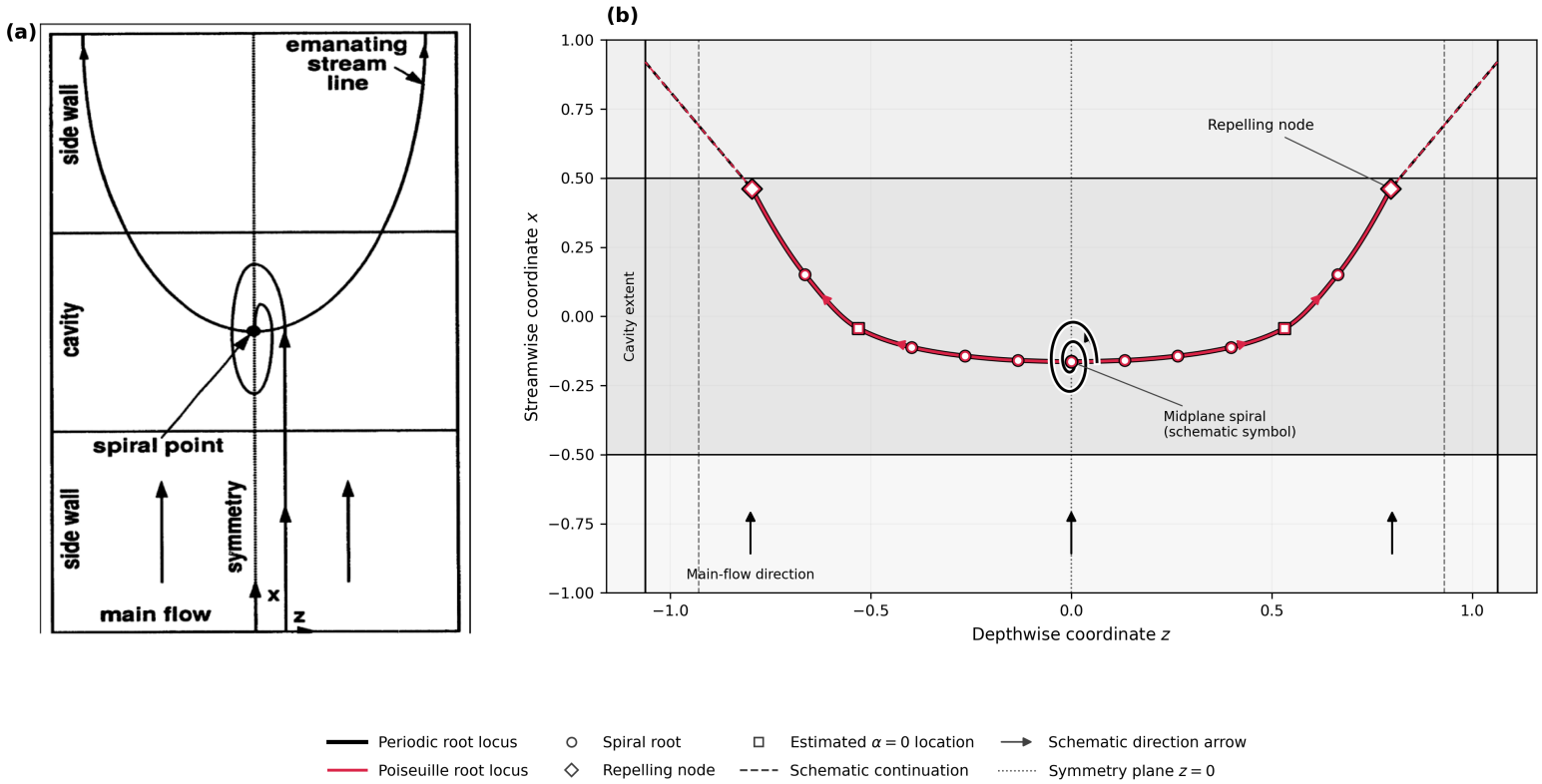


Figure 4.13: Low-Re cavity-flow comparison. (a) Schematic from Torczynski and O'Hern [10, Fig. 10]. (b) Periodic (black) and Poiseuille (red) fixed-depth root loci at Re = 10, projected onto (z, x); the red curve largely obscures the black curve. In the supplied panel, open circles mark computed roots, including the outer roots at $|z| = 0.796875$, which the numerical eigenvalues classify as nodes rather than spirals. Squares indicate estimated $\alpha = 0$ locations. Negative-depth roots are symmetry reflections. The physical sidewalls are at $|z| = 1.0625$ and the last sampling planes at $|z| = 0.9296875$; the cavity extends over $-0.5 \leq x \leq 0.5$. The spiral symbol, arrows, hatching and dashed continuations are schematic. The root loci are not integrated streamlines, and the hatching does not establish a three-dimensional flow boundary.

4.7 3D reconstruction and boundary-formulation comparison at Reynolds number 100

The higher-Re pattern involves a reorganisation of transport within the cavity, rather than simply faster circulation along the low-Re streamlines. For their higher-Re cases, Torczynski and O'Hern [10, pp. 2–3, Results; Fig. 11] describe a midplane periodic streamline approached by spiralling trajectories, an emanating stream surface extending towards two end points, and reentrant motion towards the midplane. Their description also includes a closed core streamline within each half of the recirculating region. They interpret this organisation through an analogy with two opposed rolling vortex rings and report fluid trajectories that appear to remain within an enclosed region. Their estimated transition near $\mathrm{Re} \simeq 35$ follows interpolation of the depthwise velocity gradient at the central spiral point; it is a reference observation, not an independently verified threshold for the present solutions.

The present sampled fields exhibit the corresponding reversal of the midplane sign pattern. Both formulations have repelling in-plane spirals at the five sampled depths from $z = 0$ to 0.53125, followed by attracting spirals at $z = 0.6640625$ and 0.796875. At the midplane, Eq. (4.3) associates in-plane repulsion with depthwise contraction. Fluid can therefore approach the midplane from either side while spiralling outwards within it. Together with an attracting midplane periodic streamline, this provides a local mechanism for the reentrant and emanating motion described by the paper. The identity applies at a reflection-symmetric midplane equilibrium; fixed-depth classifications away from that plane are not, by themselves, classifications of three-dimensional equilibria.

Figure 4.14 compares this interpretation with reconstructions of the two numerical fields using the same cubic interpolation, seed construction and integration procedures. Eight non-negative depth planes are used, with the negative half reconstructed by reflection symmetry. This gives a consistent comparison between the two representations, while making their depth interpolation a shared source of numerical sensitivity.

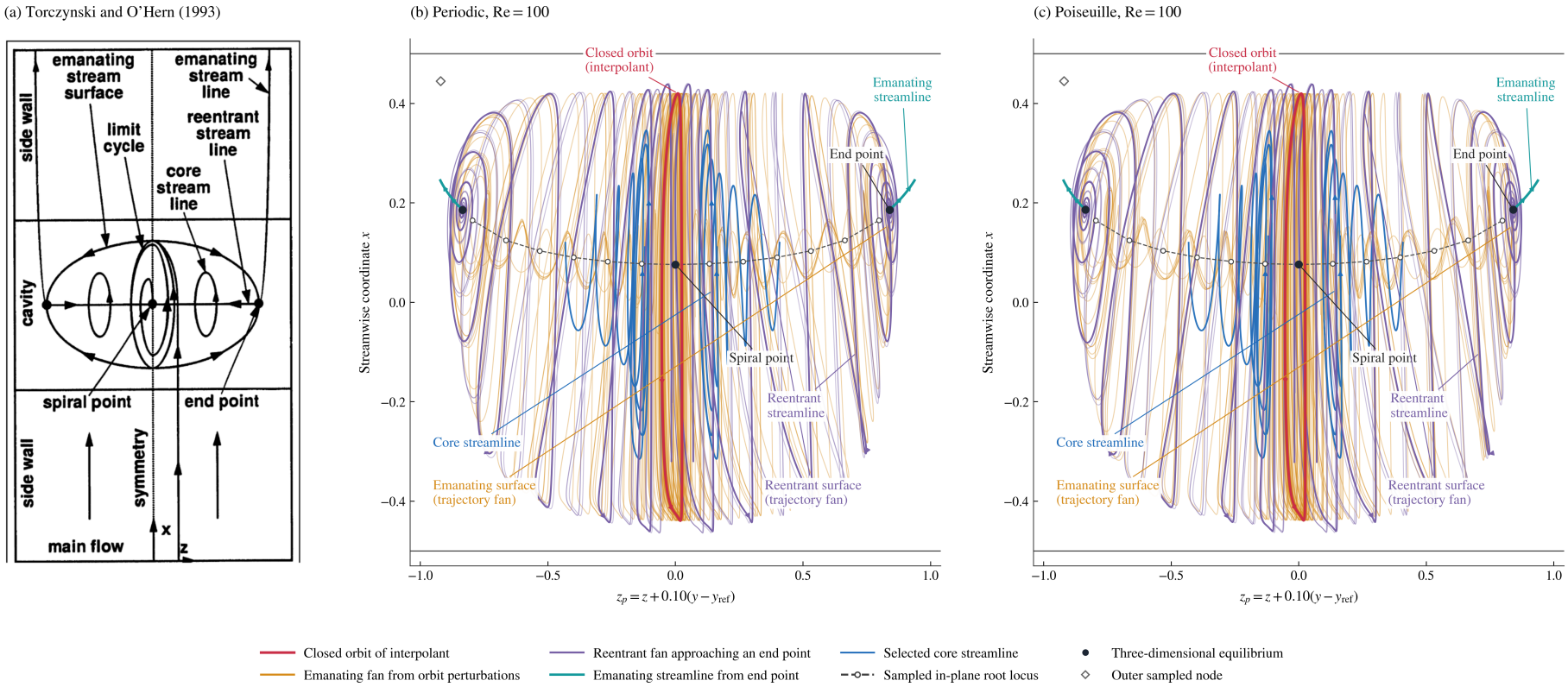


Figure 4.14: Three-dimensional cavity-flow comparison at Re = 100. (a) Qualitative schematic from Torczynski and O'Hern [10, Fig. 11]; (b) periodic and (c) Poiseuille reconstructions using the same interpolation and plotting procedures. Filled points are equilibria of the three-dimensional interpolants. Dashed curves connect sampled in-plane spiral roots; unconnected open diamonds are outer sampled nodes with non-zero depthwise velocity. Red curves are closed midplane orbits of the interpolants. Orange and purple fans sample candidate emanating and reentrant structures, while highlighted curves show selected interior, emanating and reentrant trajectories. The blue curve labelled "core" is not independently established here as the closed core streamline of the paper. Arrows denote forward flow, including on backwards-generated curves. All numerical trajectories are displayed in the common (z_p, x) projection. Curve truncation at the sampled-domain boundary is not evidence of physical escape, and the fans do not yet establish a closed invariant surface.

4.8 Preliminary one-particle Stokes results

Chapter 5

Discussion

5.1 What the background results establish

The variation of the centre-track with depth and the non-zero w^* values show why one 2D vortex is insufficient to describe the computed cavity flow. The fixed-depth plots locate and classify local structures, while 3D trajectory calculations address how fluid moves between slices. The centre-track remains a diagnostic locus throughout this interpretation.

Near the selected symmetry-plane equilibrium, the Re = 10 and 100 cases exhibit opposite combinations of in-plane and depthwise behaviour. The attraction in the plane accompanies expansion in the depth direction, and repulsion in the plane accompanies depthwise contraction. With a non-zero complex pair, both cases are 3D saddle-foci. Neither combination describes a fully attracting fluid equilibrium.

The candidate intervals in Eq. (4.2) describe a local change on the selected branch; they do not determine the onset of a global recirculation surface or periodic orbit. The high-Reynolds number reconstruction is consistent with a 3D structure, but its projected curve cases need the separate verification described in Section 4.7.

5.2 Boundary formulation and common flow scale

The common target $U_b = 1$ provides the basis for comparing the three driving conditions once each saved field passes its own bulk-flow check. It does not make the boundary value problems identical. Periodic pressure driving represents a repeated cell, whereas the inlet–outlet problems also depend on the prescribed profile, development length and downstream condition.

The matched-sample comparison at Re = 10 in Section 4.6 quantifies the close agreement of the periodic and Poiseuille representations. The outer-node displacement

between them is smaller than its interpolation sensitivity. This agreement at one source resolution does not establish equality of the boundary value problems or predict agreement at other Reynolds numbers. Their common provisional transition bracket remains a separate observation requiring branch and mesh checks.

5.3 Meaning and limitations of the particle result

5.4 Limits and next steps

Chapter 6

Conclusions and Planned Work

6.1 Conclusions from work completed to date

The project has implemented a 3D background-flow framework for the channel–cavity geometry, using the target upstream mean velocity as the reference velocity. The periodic Re = 10 medium-source field achieves $U_b = 0.9999503$ and $Q = 1.0624472$, within the stated bulk-flow tolerance, with small reported periodic and volume/classification discrepancies (Table 4.1). The revised normalisation supplies a common target for the periodic, Poiseuille and quadratic cases. These checks apply to the reported field; they do not establish source-mesh independence or certify every field used in the topology figures. Each inlet-driven field must also pass an independent bulk-flow check.

The matched-sample comparison at Re = 10 quantifies the close agreement of the periodic and Poiseuille numerical fields at the nominal base-source resolution (Section 4.6). Continuation checks distinguish the six spiral samples from an additional outer repelling node on the selected in-plane root branch. The node's position is more sensitive to interpolation than to the choice between these two boundary formulations. These results support agreement of the sampled representations, with source-mesh and sampling refinement still required.

The topological analysis distinguishes fixed-depth diagnostics from 3D fluid trajectories. Near the selected symmetry-plane equilibrium, the periodic Re = 10 field is locally attracting in-plane with depthwise motion away from the plane, whereas the Re = 100 field shows the opposite combination. The local-transition intervals are reported in Eq. (4.2). They remain provisional pending branch-continuity, derivative and numerical uncertainty checks. The closed background-fluid orbits reported in Section 4.7 belong to the interpolated fields; their persistence in the underlying flow remains unverified. A global bifurcation and finite-particle retention have not been established.

6.2 Staged research plan and validation gates

6.3 Expected research outputs

The first planned paper will address background-flow verification, the comparison of boundary formulations at a common target mean velocity, and Reynolds-number-dependent cavity-flow topology. Its conclusions will distinguish the established sampled-field comparisons from transition or global-structure claims that require further verification.

The second planned paper will present the cavity-specific particle formulation and its numerical verification and physical validation. Migration maps and outcome classification will be included after the inertial correction and trajectory model satisfy the stated acceptance criteria.

The thesis will connect a background field with quantified numerical uncertainty, a particle-response model with a stated domain of validity, and trajectories classified by explicit passage, entry, residence, retention and release criteria. This sequence provides a testable route from the completed flow and Stokes calculations to the investigation of size-dependent particle behaviour in the cavity–channel device.

Bibliography

[1] M. Toner and D. Irimia, "Blood-on-a-chip," *Annu. Rev. Biomed. Eng.*, vol. 7, pp. 77–103, 2005, doi: 10.1146/annurev.bioeng.7.011205.135108.

[2] M. E. Warkiani, G. Guan, B. L. W. C. Luan, Khoo, A. A. S. Bhagat, and j. . L. v. . . n. . . p. . . y. . . d. . C. n. . doi: 10.1039/C3LC50617G. Chaudhuri, Parthiv Kant and Tan, Daniel Shao-Weng and Lim, Wan Teck and Lee, Soo Chin and Chen, Peter C. Y. and Lim, Chwee Teck and Han, Jongyoon, title = Slanted spiral microfluidics for the ultra-fast, label-free isolation of circulating tumor cells.

[3] D. Di Carlo, "Inertial microfluidics," *Lab Chip*, vol. 9, no. 21, pp. 3038–3046, 2009, doi: 10.1039/B912547G.

[4] G. Segré and A. Silberberg, "Behaviour of macroscopic rigid spheres in Poiseuille flow. part 2. experimental results and interpretation," *J. Fluid Mech.*, vol. 14, no. 1, pp. 136–157, 1962, doi: 10.1017/S0022112062001111.

[5] B. P. Ho and L. G. Leal, "Inertial migration of rigid spheres in two-dimensional unidirectional flows," *J. Fluid Mech.*, vol. 65, no. 2, pp. 365–400, 1974, doi: 10.1017/S0022112074001431.

[6] K. Hood, S. Lee, and M. Roper, "Inertial migration of a rigid sphere in three-dimensional Poiseuille flow," *J. Fluid Mech.*, vol. 765, pp. 452–479, 2015, doi: 10.1017/jfm.2014.739.

[7] S. C. Hur, A. J. Mach, and D. Di Carlo, "High-throughput size-based rare cell enrichment using microscale vortices," *Biomicrofluidics*, vol. 5, no. 2, 2011, Art. no. 022206, doi: 10.1063/1.3576780.

[8] A. J. Mach, J. H. Kim, A. Arshi, S. C. Hur, and D. Di Carlo, "Automated cellular sample preparation using a centrifuge-on-a-chip," *Lab Chip*, vol. 11, no. 17, pp. 2827–2834, 2011, doi: 10.1039/C1LC20330D.

[9] S. Christensen and M. Roper, "Inertial migration in micro-centrifuge devices," arXiv preprint arXiv:2303.06760, 2023, doi: 10.48550/arXiv.2303.06760.

[10] J. R. Torczynski and T. J. O'Hern, "Numerical simulations of flow in a three-dimensional cavity-channel geometry," Sandia National Laboratories, Albuquerque, NM, USA, Tech. Rep. SAND93-1439C, 1993. [Online]. Available: https://www.osti.gov/biblio/10103289

[11] R. Khojah, D. Lo, F. Tang, and D. Di Carlo, "The evolution of flow and mass transport in 3D confined cavities," arXiv preprint arXiv:2101.07242, 2021, doi: 10.48550/arXiv.2101.07242.

[12] P. G. Saffman, "The lift on a small sphere in a slow shear flow," *J. Fluid Mech.*, vol. 22, no. 2, pp. 385–400, 1965, doi: 10.1017/S0022112068999990.

[13] J. A. Schonberg and E. J. Hinch, "Inertial migration of a sphere in Poiseuille flow," *J. Fluid Mech.*, vol. 203, pp. 517–524, 1989, doi: 10.1017/S0022112089001564.

[14] P. G. Saffman, "The lift on a small sphere in a slow shear flow—corrigendum," *Journal of Fluid Mechanics*, vol. 31, no. 3, p. 624, 1968.

[15] R. G. Cox and H. Brenner, "The lateral migration of solid particles in Poiseuille flow—I. theory," *Chem. Eng. Sci.*, vol. 23, no. 2, pp. 147–173, 1968, doi: 10.1016/0009-2509(68)87059-9.

[16] P. Vasseur and R. G. Cox, "The lateral migration of a spherical particle in two-dimensional shear flows," *J. Fluid Mech.*, vol. 78, no. 2, pp. 385–413, 1976, doi: 10.1017/S0022112076002498.

[17] E. S. Asmolov, "The inertial lift on a spherical particle in a plane Poiseuille flow at large channel Reynolds number," *J. Fluid Mech.*, vol. 381, pp. 63–87, 1999, doi: 10.1017/S0022112098003474.

[18] S. H. Strogatz, *Nonlinear Dynamics and Chaos: With Applications to Physics, Biology, Chemistry, and Engineering*, 2nd ed. CRC Press, 2018, doi: 10.1201/9780429492563.

[19] H. Haddadi and D. Di Carlo, "Inertial flow of a dilute suspension over cavities in a microchannel," *J. Fluid Mech.*, vol. 811, pp. 436–467, 2017, doi: 10.1017/jfm.2016.709.

[20] M. Jiang, S. Qian, and Z. Liu, "Fully resolved simulation of single-particle dynamics in a microcavity," *Microfluid. Nanofluid.*, vol. 22, no. 12, 2018, Art. no. 144, doi: 10.1007/s10404-018-2166-x.

[21] S. Christensen, R. Chu, C. Anderson, and M. Roper, "Fast asymptotic-numerical method for coarse mesh particle simulation in channels of arbitrary cross section," *J. Comput. Phys.*, vol. 471, 2022, Art. no. 111622, doi: 10.1016/j.jcp.2022.111622.

[22] G. K. Batchelor, *An Introduction to Fluid Dynamics*, ser. Cambridge Mathematical Library. Cambridge University Press, 2000, reissue of the work first published in 1967, doi: 10.1017/CBO9780511800955.

[23] H. Hasimoto, "On the periodic fundamental solutions of the Stokes equations and their application to viscous flow past a cubic array of spheres," *Journal of Fluid Mechanics*, vol. 5, no. 2, pp. 317–328, 1959.

[24] S. V. Patankar, C. H. Liu, and E. M. Sparrow, "Fully developed flow and heat transfer in ducts having streamwise-periodic variations of cross-sectional area," *J. Heat Transf.*, vol. 99, no. 2, pp. 180–186, 1977, doi: 10.1115/1.3450666.

[25] S. B. Beale, "On the implementation of stream-wise periodic boundary conditions," in *Proceedings of the 2005 ASME Summer Heat Transfer Conference*. ASME, 2005, pp. 771–777, doi: 10.1115/HT2005-72271.

[26] M. Neunteufel and J. Schöberl, "Fluid-structure interaction with $H(\mathrm{div})$-conforming finite elements," *Computers & Structures*, vol. 243, p. 106402, 2021.

[27] N. A. Mortensen, F. Okkels, and H. Bruus, "Reexamination of Hagen–Poiseuille flow: Shape dependence of the hydraulic resistance in microchannels," *Physical Review E*, vol. 71, no. 5, 2005, Art. no. 057301, doi: 10.1103/PhysRevE.71.057301.

[28] C. Geuzaine and J.-F. Remacle, "Gmsh: A 3-D finite element mesh generator with built-in pre- and post-processing facilities," *Int. J. Numer. Methods Eng.*, vol. 79, no. 11, pp. 1309–1331, 2009, doi: 10.1002/nme.2579.

[29] B. Krauskopf *et al.*, "A survey of methods for computing (un)stable manifolds of vector fields," *Int. J. Bifurcation Chaos*, vol. 15, no. 3, pp. 763–791, 2005, doi: 10.1142/S0218127405012533.

[30] S. Kim and S. J. Karrila, *Microhydrodynamics: Principles and Selected Applications*. Boston, MA, USA: Butterworth-Heinemann, 1991, doi: 10.1016/C2013-0-04644-0.

[31] H. Masoud and H. A. Stone, "The reciprocal theorem in fluid dynamics and transport phenomena," *J. Fluid Mech.*, vol. 879, 2019, Art. no. P1, doi: 10.1017/jfm.2019.553.